

Deep Metric Imitation Learning for Stable Motion Primitives

Rodrigo Pérez-Dattari¹, Cosimo Della Santina¹, and Jens Kober¹

¹Department of Cognitive Robotics, Delft University of Technology, The Netherlands

Abstract— Imitation Learning (IL) is a powerful technique for intuitive robotic programming. However, ensuring the reliability of learned behaviors remains a challenge. In the context of reaching motions, a robot should consistently reach its goal, regardless of its initial conditions. To meet this requirement, IL methods often employ specialized function approximators that guarantee this property by construction. Although effective, these approaches come with a set of limitations: 1) they are unable to fully exploit the capabilities of modern Deep Neural Network (DNN) architectures, 2) some are restricted in the family of motions they can model, resulting in suboptimal IL capabilities, and 3) they require explicit extensions to account for the geometry of motions that consider orientations. To address these challenges, we introduce a novel stability loss function, drawing inspiration from the triplet loss used in the deep metric learning literature. This loss does not constrain the DNN’s architecture and enables learning policies that yield accurate results. Furthermore, it is not restricted to a specific state space geometry; therefore, it can easily incorporate the geometry of the robot’s state space. We provide a proof of the stability properties induced by this loss and empirically validate our method in various settings. These settings include Euclidean and non-Euclidean state spaces, as well as first-order and second-order motions, both in simulation and with real robots. More details about the experimental results can be found in: <https://youtu.be/ZWKLgntCI6w>.

Keywords— *Imitation Learning, Deep Metric Learning, Dynamical Systems, Motion Primitives, Deep Neural Networks, non-Euclidean geometry*

1 Introduction

Imitation Learning (IL) provides a powerful framework for the intuitive programming of robotic systems. Its strength lies in its ability to leverage human-like learning methodologies, such as demonstrations and corrections, making it accessible to non-robotics experts. This attribute significantly reduces the resources needed to build robotic systems. However, the data-driven nature of these methodologies presents a challenge: providing guarantees about the learned behaviors.

In the context of reaching motions, it is crucial for the robot’s motions to consistently reach the intended target, irrespective of the robot’s initial conditions. Thus, modeling motions as dynamical systems proves beneficial. This approach turns the problem into a question of ensuring *global asymptotic stability* (or *stability*, for short) at the goal, and tools from dynamical system theory can then be applied to guarantee this property.

Numerous methods have been proposed to ensure stability in motions represented by dynamical systems. However, they often exhibit at least one of the following limitations: 1) constraining the structure of their function approximators, and/or 2) being designed with the assumption that the robot’s state space is Euclidean. To elaborate:

1. **Constrained function approximators.** To ensure stability guarantees, methods often constrain the structure

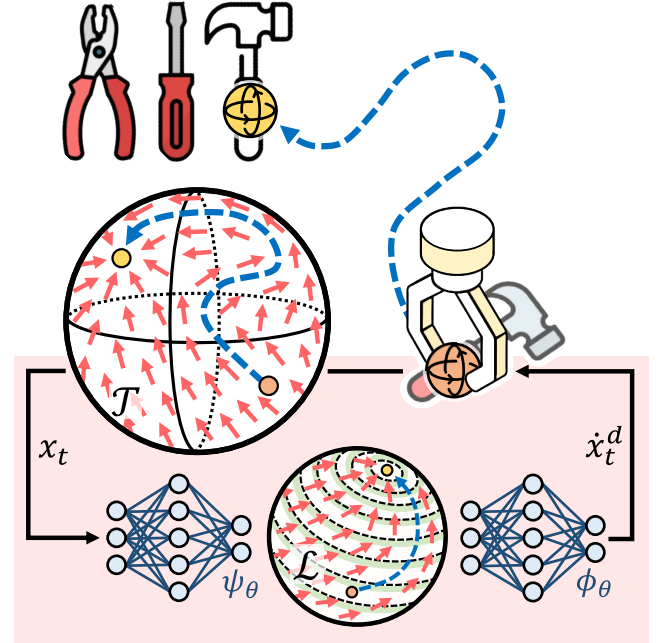


Figure 1: Motion learned using the proposed framework. The blue trajectory in the task space \mathcal{T} demonstrates the evolution of the robot’s end effector state x_t when represented in a spherical manifold. The evolution of this trajectory is governed by the dynamical system $\dot{x}_t = \phi_\theta(\psi_\theta(x_t))$, depicted as a vector field of red arrows in the remaining of the space. Through Deep Metric Learning, this system is stabilized by deriving a simpler representation in the latent space \mathcal{L} .

of their function approximators. For instance, some approaches necessitate invertibility [1, 2, 3], while others require positive or negative definiteness [4, 5, 6]. However, these methods do not enable full exploitation of modern Deep Neural Network (DNN) architectures, as these constraints are not typically present in DNNs. This limitation hinders their broader application in more complex models, where integrating these constraints is challenging. Furthermore, inherently constraining function approximators can overly restrict the range of solutions to which they can converge, resulting in less flexible models than necessary. This leads to suboptimal IL capabilities. In our context, this problem is known as the *stability versus accuracy dilemma* [7].

2. **Euclidean assumption.** Learned motions must integrate with the geometry of the space used to represent a robot’s state. For example, the end-effector of a manipulator should always reach the intended target in both position and orientation space. However, orientations are often represented in non-Euclidean spaces, such as $SO(3)$ or \mathcal{S}^3 . This is because Euclidean representations like Euler angles may not always provide a continuous description of motions that

are inherently continuous² [8]. Such continuity is often a requirement for motions modeled as dynamical systems. Furthermore, the generalization capabilities of function approximations are compromised by non-continuous representations. To enable proper generalization, states that are close in the real world should be represented as closely related in the function approximator’s input, i.e., the state space representation.

Nevertheless, previous methods for stable motion generation have been initially designed under the assumption that the state space is Euclidean [4, 2, 3, 9]. Consequently, some have later been explicitly adapted to account for the geometry of motions that consider orientations [10, 11, 12], resulting in rather convoluted learning frameworks.

In this work, we present a DNN framework capable of learning accurate stable motions in state spaces with arbitrary geometries, without constraining the DNN’s architecture. To accomplish this, we introduce a novel loss function that repurposes the *triplet loss*, commonly used in deep metric learning literature [13, 14]. We prove that this loss imposes conditions on the DNN’s latent space that enforce the learned dynamical system to have a globally asymptotically stable equilibrium at the goal. To account for the geometry of the state space, it is sufficient to consider its corresponding metric during the computation of the loss, the choice of which depends on the specific task at hand. We validate our method in various settings, including Euclidean, non-Euclidean, first-order, and second-order motions. Additionally, real-world experiments that control the 7-dimensional pose (x-y-z position and quaternion orientation) of a robotic manipulator’s end effector demonstrate the method’s practical applicability and potential.

The rest of this paper offers a thorough discussion of these developments. Following a review of the relevant literature, we delve into foundational concepts and problem formulation. We then present the details of our methodology, provide a proof regarding the stability of the learned motion, and discuss the integration of the triplet loss function within the context of non-Euclidean state representations. We validate our approach through several experiments and conclude by considering potential directions for future research based on our findings.

2 Related Works

Three categories of works are relevant to this paper. First, there are papers that focus on learning stable motions, assuming these motions occur in Euclidean state spaces. Second, others explore learning motions in non-Euclidean state spaces, but do not consider the stability of the learned motions. Finally, a third set of papers addresses both learning motions in non-Euclidean state spaces and their stability.

In every case, works use either *time-varying/non-autonomous* or *time-invariant/autonomous* dynamical systems for motion modeling. In time-varying systems, evolution explicitly depends on time (or a phase). Conversely, time-invariant systems

do not directly depend on time; instead, they rely on their time-varying input (i.e., the state of the system). The property of a system being time-invariant or not dictates the strategies we can use to ensure its stability. Thus, making a distinction between these systems is important. Notably, both types of formulations have been shown to be complementary in the context of IL [15, 16].

This work focuses on time-invariant dynamical systems. Consequently, although we consider both methodologies for motion learning, we delve deeper into the literature on time-invariant systems for IL.

2.1 Stability in Euclidean State Spaces

Regarding time-varying dynamical systems, a seminal work in IL that addresses the problem of learning stable motions introduces Dynamical Movement Primitives (DMPs) [17]. DMPs take advantage of the time-dependency (via the phase of the *canonical system*) of the dynamical system to make it evolve into a simple and well-understood system as time goes to infinity. The simple system is designed to be stable by construction. As a consequence, the stability of the learned motions can be guaranteed. This concept has been extended in multiple ways, for instance through probabilistic formulations [18, 19], or adapted to the context of DNNs [20, 21, 22].

Conversely, IL approaches based on time-invariant dynamical systems often constrain the function approximator used to model the dynamical systems. Such constraints ensure stability by construction. One seminal work introduces the Stable Estimator of Dynamical Systems (SEDS) [4]. This approach imposes constraints on the structure of a Gaussian Mixture Regression (GMR) such that the conditions for Lyapunov stability are always met. Multiple extensions of SEDS have been proposed, for instance by using physically-consistent priors [23], contraction theory [24] or diffeomorphisms [25].

Other works propose explicitly learning Lyapunov functions that are consistent with the demonstrations. These functions are then used to correct the transitions learned by the dynamical systems, ensuring that they are always stable according to the learned Lyapunov functions [5, 6, 26]. Moreover, some papers have employed concepts such as contraction metrics [27, 28] and diffeomorphisms [1, 2, 3, 29] to impose stability, in the sense of Lyapunov, in time-invariant dynamical systems.

Understandably, all of these methods constrain some part of their learning framework to ensure stability. From one perspective, this is advantageous as it guarantees stability. However, in many cases, this comes at the expense of reduced accuracy in the learned motions. Notably, some recent methods have managed to mitigate this loss in accuracy [2, 3]. Nevertheless, they are still limited in terms of the family of models that can be used with these frameworks, which harms their scalability.

In previous work [9], we addressed this issue by applying tools from the deep metric learning literature [14]. In this context, we introduced CONDOR, which uses a *contrastive loss* to enforce stability in learned motions through the optimization process of a DNN. This approach proved effective in learning stable, accurate, and scalable motions from human demonstrations. However, this method presents two limitations. First, it requires the design of a stable and well-understood system for

²These limitations arise from singularities in these models, also known as *gimbal lock*, as well as non-unique representations.

computing the contrastive loss (referred to as $f^{\mathcal{L}}$ in Sec. 3.3), which can significantly impact learning performance. Therefore, it would be advantageous to have a loss that does not depend on $f^{\mathcal{L}}$. Second, like the other methods introduced in this subsection, CONDOR is restricted to working in Euclidean state spaces.

In this work, we introduce a novel deep metric learning loss that ensures stability while addressing the limitations of [9], specifically, the need for the function $f^{\mathcal{L}}$ and the inability to learn motions in non-Euclidean manifolds.

2.2 Stability in Non-Euclidean State Spaces

As noted previously, it is crucial to consider the geometry of our state spaces when learning motions requiring pose control. Consequently, many studies have adapted methods that originally assumed data from Euclidean spaces to work with data from non-Euclidean manifolds, such as $SO(3)$ and S^3 . In the context of IL, pioneering approaches utilized time-varying dynamical systems (extensions of DMPs) to incorporate the geometry of orientation representations into their models [30, 8, 31]. Because DMPs inherently ensure stability, these methods are stable as well.

In contrast, although several geometry-aware IL approaches based on time-invariant dynamical systems have been introduced, such as Gaussian process regressions [32, 33], GMRs [34, 35, 36, 37], and kernelized movement primitives [38, 39], such methods are not inherently stable. As a result, in these cases, models need to be explicitly endowed with stability properties. This limitation has been addressed in recent works, where [40] uses GMRs and employs contraction theory to ensure stability considering the robot’s orientation geometry. Furthermore, recent methods have extended the use of diffeomorphism-based techniques for stability to generate motions in non-Euclidean manifolds as well [10, 11, 12].

These diffeomorphism-based methods are of particular interest to our work, as our method is grounded in similar concepts for achieving stability. In both approaches, we transfer the stability properties of a simple system in the latent space of a DNN to the dynamical system that models motion in task space. However, unlike these other methods, our approach learns this property, while the other works constrain the DNN structure to ensure its satisfaction. Moreover, our method allows us to effortlessly incorporate the geometrical aspects of the robot’s state space into the learned model, as this is factored into the optimization process of the DNN.

3 Preliminaries

3.1 Dynamical Systems for Reaching Tasks

In this work, we model motions as solutions of nonlinear time-invariant dynamical systems represented by

$$\dot{x} = f(x), \quad (1)$$

where $x \in \mathcal{T}$, with $\mathcal{T} \subset \mathbb{R}^n$, is the state, and $f : \mathcal{T} \rightarrow \mathbb{R}^n$ is a differentiable function. Since we are interested in solving reaching tasks, we aim to construct systems with a globally

asymptotically stable equilibrium at x_g . This implies that

$$\lim_{t \rightarrow \infty} \|x_g - x\| = 0, \quad \forall x \in \mathcal{T}.$$

3.2 Problem Formulation

We consider a robot learning a reaching motion in the space \mathcal{T} towards the goal state $x_g \in \mathcal{T}$, based on a set of demonstrations \mathcal{D} . The robot is expected to imitate the behavior shown in the demonstrations while always reaching x_g , regardless of its initial state. The dataset \mathcal{D} contains N trajectories τ_i showing the evolution of a dynamical system’s state x_t from an initial state x_0 with T samples obtained at different times t .

We assume that these demonstrations are drawn from the distribution $p^*(\tau)$, following the *optimal* dynamical system f^* (according to the demonstrator’s judgment). On the other hand, the robot’s motion follows the parametrized system $f_\theta^{\mathcal{T}}$, inducing the distribution $p_\theta(\tau)$, where θ is the parameter vector. The objective is to find θ^* that minimizes the difference, expressed as the (forward) Kullback-Leibler divergence, between the trajectory distributions, while ensuring that x_g is a globally asymptotically stable equilibrium:

$$\begin{aligned} \theta^* = \arg \min_{\theta \in \Theta} \quad & D_{\text{KL}}(p^*(\tau) || p_\theta(\tau)) \\ \text{s.t.} \quad & \lim_{t \rightarrow \infty} d(x_g, x_t) = 0, \forall x_t \in \mathcal{T} \end{aligned} \quad (2a)$$

where Θ is the parameter space of a DNN and $d(\cdot, \cdot)$ is a distance function.

3.3 Stability Conditions

In [9], the *stability conditions* were formulated to enforce stability in $f_\theta^{\mathcal{T}}$. The objective is to ensure that $f_\theta^{\mathcal{T}}$ inherits the stability properties from a simple and stable system, referred to as $f^{\mathcal{L}}$. Thus, if $f^{\mathcal{L}}$ is stable, $f_\theta^{\mathcal{T}}$ will also be stable. To achieve this, we require $f^{\mathcal{L}}$ to reside within the output of one of the hidden layers of the DNN that parameterizes $f_\theta^{\mathcal{T}}$. As such, we express the dynamical system $f_\theta^{\mathcal{T}}$ as a composition of two functions, ψ_θ and ϕ_θ ,

$$\dot{x}_t = f_\theta^{\mathcal{T}}(x_t) = \phi_\theta(\psi_\theta(x_t)).$$

However, $f_\theta^{\mathcal{T}}$ is a standard DNN with L layers. ψ_θ denotes layers $1, \dots, l$, and ϕ_θ layers $l+1, \dots, L$. We define the output of layer l as the latent space $\mathcal{L} \subset \mathbb{R}^m$. Note that $\mathcal{L} \subset \mathbb{R}^m$ implies the dimensionality of the vectors used to represent \mathcal{T} and \mathcal{L} **does not need to be the same**. Moreover, for simplicity, although we use the same θ notation for both ψ_θ and ϕ_θ , each symbol actually refers to a different subset of parameters within θ . These subsets together form the full parameter set in $f_\theta^{\mathcal{T}}$.

Additionally, we need to introduce a third dynamical system. This system denotes the evolution in \mathcal{L} of the states visited by $f_\theta^{\mathcal{T}}$ when mapped using ψ_θ , which yields the relationship

$$\dot{y}_t = f_\theta^{\mathcal{T} \rightarrow \mathcal{L}}(x_t) = \frac{\partial \psi_\theta(x_t)}{\partial t},$$

$\forall y_t \in \mathcal{L}$, where y_t corresponds to the latent variables that evolve according to $f_\theta^{\mathcal{T} \rightarrow \mathcal{L}}$. Fig. 2 provides an example of the introduced dynamical systems.

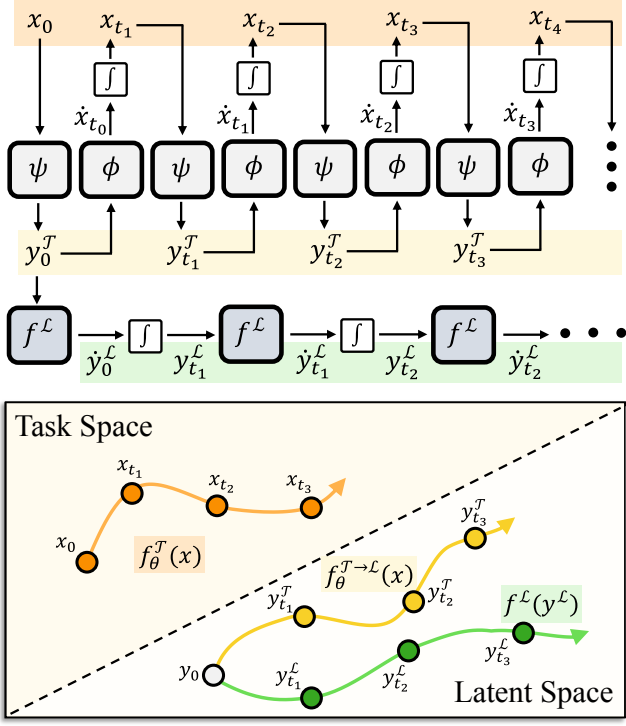


Figure 2: Example of trajectories generated by simulating the systems f_θ^T , $f_\theta^{T \rightarrow \mathcal{L}}$ and $f^\mathcal{L}$ for different time instants using the forward Euler method. Importantly, the stability conditions are not met in this case, because $f_\theta^{T \rightarrow \mathcal{L}}$ differs from $f^\mathcal{L}$.

Then, the stability conditions of [9] can be written as:

Theorem 1 (Stability conditions: v1). *Let f_θ^T , $f_\theta^{T \rightarrow \mathcal{L}}$ and $f^\mathcal{L}$ be the introduced dynamical systems. Then, in the region \mathcal{T} , x_g is a globally asymptotically stable equilibrium of f_θ^T if, $\forall x_t \in \mathcal{T}$:*

1. $f_\theta^{T \rightarrow \mathcal{L}}(x_t) = f^\mathcal{L}(y_t)$,
2. $\psi_\theta(x_t) = y_g \Rightarrow x_t = x_g$.

In this work, we reformulate these conditions and propose a novel loss for optimizing them. This adaptation endows the learning framework with increased flexibility, enabling it to tackle a wider array of problems (e.g., non-Euclidean state spaces) and achieve improved performance.

3.4 Deep Metric Learning: the Triplet Loss

Commonly employed in the Deep Metric Learning literature, the *triplet loss* [13] has been utilized for learning and structuring latent state representations [14]. Its function is to cluster similar observations together and differentiate dissimilar ones within the latent space of a DNN. In this work, however, the triplet loss is used differently. Although we continue to use this loss to impose a certain structure on the DNN’s latent space, its goal is to do so in a specific manner that enforces stability in f_θ^T , achieved by satisfying the stability conditions.

Let us recall the triplet loss:

$$\ell_{\text{triplet}} = \max(0, m + d(a, p) - d(a, n)),$$

where $m \in \mathbb{R}_{>0}$ is the margin, a is the anchor sample, p the positive sample, and n the negative sample. This loss enforces

positive samples to be at least m distance closer to the anchor than the negative samples. Importantly, note that this is enough for the loss to become zero; it does not require the anchor and the positive sample to have the same value.

3.5 Stability Analysis through Comparison Functions

We employ comparison functions, namely class- \mathcal{KL} functions, to prove that the proposed method, based on the triplet loss, enforces global asymptotic stability at the equilibrium x_g . These functions are used to formulate a general approach for stability analysis in the sense of Lyapunov. As described in [41, 42], these functions are defined as follows:

Definition 1 (class- \mathcal{K} function). A continuous function $\alpha : [0, a) \rightarrow \mathbb{R}_{\geq 0}$, for $a \in \mathbb{R}_{>0}$, is said to belong to class \mathcal{K} if it is strictly increasing and $\alpha(0) = 0$.

Definition 2 (class- \mathcal{L}^3 function). A continuous function $\sigma : \mathbb{R}_{\geq 0} \rightarrow \mathbb{R}_{>0}$, is said to belong to class \mathcal{L} if it is *weakly decreasing*⁴ and $\lim_{s \rightarrow \infty} \sigma(s) = 0$.

Definition 3 (class- \mathcal{KL} function). A function $\beta : [0, a) \times \mathbb{R}_{\geq 0} \rightarrow \mathbb{R}_{\geq 0}$, for $a \in \mathbb{R}_{>0}$, is said to belong to class \mathcal{KL} if:

- for each fixed s , the mapping $\beta(r, s)$ belongs to class- \mathcal{K} with respect to r ,
- for each fixed r , the mapping $\beta(r, s)$ belongs to class- \mathcal{L} with respect to s .

Then, we can describe global asymptotic stability in terms of class- \mathcal{KL} functions as:

Theorem 2 (Global asymptotic stability with class- \mathcal{KL} functions). *The state x_g is a globally asymptotically stable equilibrium of (1) in \mathcal{T} if there exists a class- \mathcal{KL} function β such that, $\forall t \in \mathbb{R}_{\geq 0}$ and $\forall x_0 \in \mathcal{T}$,*

$$\|x_g - x_t\| \leq \beta(\|x_g - x_0\|, t). \quad (3)$$

Note that this theorem seamlessly integrates the concepts of *stability* and *attractivity* within a single function β , which acts as an upper bound of $\|x_g - x_t\|$. As the initial condition of the system moves further away from x_g , β correspondingly increases. Moreover, as the system evolves over time and β decreases, it follows that the system’s distance to x_g will eventually decrease.

4 Methodology

We aim to learn motions from demonstrations, which are modeled as nonlinear time-invariant dynamical systems. In this context, we introduce the *Policy via neUral Metric leArning*

³Please note that there is a distinction in the use of the symbol \mathcal{L} . While it represents the class- \mathcal{L} functions, it is also used to denote the set \mathcal{L} introduced in Sec. 3.3. In subsequent sections of the paper, the \mathcal{L} referring to class- \mathcal{L} functions is exclusively used in the form \mathcal{KL} .

⁴We use this term to denote functions that either remain constant or strictly decrease within any interval of their domain. While these functions are often referred to as *decreasing* or *non-increasing*, we find these terms potentially ambiguous.

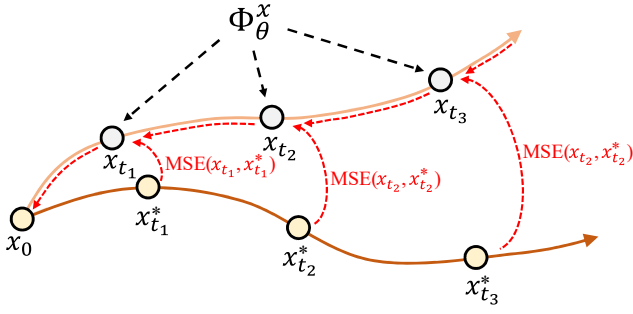


Figure 3: Illustration of the behavioral cloning loss computation. Starting from an initial condition x_0 , the system f_θ^T evolves to various time instants via Φ_θ^x . At each instant, the estimated state is compared with a demonstrated state. The red arrows show the path used to update the DNN weights using BPTT, for each x_t as a function of x_0 .

(PUMA) framework, which learns the parametrized function f_θ^T from human demonstrations. Furthermore, it guarantees that the goal of the motion x_g is a globally asymptotically stable equilibrium of this dynamical system, while maintaining accuracy with respect to the demonstrations. To achieve this, we augment the Imitation Learning (IL) problem with the loss ℓ_{stable} designed to enforce stability in the learned dynamical system based on the triplet loss. Hence, our framework minimizes:

$$\ell_{\text{TIL}} = \ell_{\text{IL}} + \lambda \ell_{\text{stable}}, \quad (4)$$

where $\lambda \in \mathbb{R}_{>0}$ is a weight factor. We denote ℓ_{TIL} as the *Triplet Imitation Learning* (TIL) loss.

4.1 Behavioral Cloning

To minimize ℓ_{IL} , and thereby address (2a), we adopt the behavioral cloning loss used in [9]. This loss enables the optimization of a deterministic value by representing the dynamical system as the mean of a Gaussian distribution with a fixed covariance. Furthermore, it mitigates *covariate shift* by minimizing the multi-step error over trajectory segments \mathcal{H}^i using *backpropagation through time* (BPTT).

In every training iteration, we sample a batch \mathcal{B}^i of trajectory segments \mathcal{H}^i from the dataset \mathcal{D} . These segments can start at any point within a given demonstration, with the start time defined as $t = 0$. Then, by introducing the *evolution function* $\Phi_\theta^x(t, x_0) : \mathbb{R}_{\geq 0} \times \mathcal{T} \rightarrow \mathcal{T}$, which defines the estimated value of x_t by integrating f_θ^T between 0 and t , with initial condition x_0 , we have

$$\ell_{\text{IL}} = \sum_{\mathcal{H}^i \in \mathcal{B}^i} \sum_{(t, x_t^*) \in \mathcal{H}^i} \|x_t^* - \Phi_\theta^x(t, x_0)\|_2^2,$$

where the states x_t^* along the trajectory segment \mathcal{H}^i serve as labels for the states predicted by the DNN from the initial condition x_0 using $\Phi_\theta^x(t, x_0)$. Note that the initial condition is obtained from \mathcal{H}^i , i.e., $x_0 = x_0^*$. Fig. 3 illustrates the computation of this loss for one trajectory.

Since we do not have an analytical solution of Φ_θ^x , we approximate it using the *forward Euler method*, i.e.,

$$\Phi_\theta^x(t, x_0) = \Phi_\theta^x(t', x_0) + f_\theta^T(\Phi_\theta^x(t', x_0)) \Delta t,$$

where $t' = t - \Delta t$ and $\Delta t \in \mathbb{R}_{>0}$ is the time step size. This integration starts with the initial state x_0 , i.e., $\Phi_\theta^x(0, x_0) = x_0$. It is important to note that the recursive nature of $\Phi_\theta^x(t, x_0)$ necessitates the use of BPTT for the optimization of the DNN.

4.2 Triplet Stability Loss

4.2.1 Reformulating the Stability Conditions

The stability conditions of Theo. 1 involve three dynamical systems: f_θ^T , $f_\theta^{T \rightarrow \mathcal{L}}$, and $f^\mathcal{L}$. Note, however, that its first condition, namely $f_\theta^{T \rightarrow \mathcal{L}} = f^\mathcal{L} \forall x_t \in \mathcal{T}$, essentially states that $f_\theta^{T \rightarrow \mathcal{L}}$ must exhibit global asymptotic stability. In other words, if the behavior of $f_\theta^{T \rightarrow \mathcal{L}}$ is identical to that of another system, $f^\mathcal{L}$, for which stability is verified, then the stability of $f_\theta^{T \rightarrow \mathcal{L}}$ is also verified. Nonetheless, if we can verify its stability through a different method, these conditions can be more generally written as follows:

Theorem 3 (Stability conditions: v2). *Let f_θ^T and $f_\theta^{T \rightarrow \mathcal{L}}$ be the introduced dynamical systems. Then, in the region \mathcal{T} , x_g is a globally asymptotically stable equilibrium of f_θ^T if, $\forall x_t \in \mathcal{T}$:*

1. y_g is a globally asymptotically stable equilibrium of $f_\theta^{T \rightarrow \mathcal{L}}(x_t)$,
2. $\psi_\theta(x_t) = y_g \Rightarrow x_t = x_g$.

4.2.2 Surrogate Stability Conditions

Theo. 3 introduces two conditions. If these are met within f_θ^T , the system will possess a globally asymptotically stable equilibrium at x_g . However, these conditions do not offer a method for optimizing DNNs in a manner that ensures their fulfillment. Therefore, we introduce the *surrogate stability conditions* of Theo. 3. These conditions, when met, imply that the stability conditions of Theo. 3 are satisfied. Unlike the stability conditions, the surrogate conditions can be transformed into a loss function for optimizing the DNN, namely ℓ_{stable} , which enforces their satisfaction.

To formulate the surrogate stability conditions, we note that Theo. 3 can be expressed in terms of relative distances. To facilitate this, we define the distance between any given latent state y_t and a fixed target state y_g as $d_t = d(y_g, y_t) = \|y_g - y_t\|$. Then, we formally introduce the conditions as:

Theorem 4 (Surrogate stability conditions). *Let two dynamical systems be governed by the equations $\dot{x}_t = f_\theta^T(x_t)$ and $\dot{y}_t = f_\theta^{T \rightarrow \mathcal{L}}(y_t)$, such that $y_t = \psi_\theta(x_t)$. Assume both f_θ^T and $f_\theta^{T \rightarrow \mathcal{L}}$ are continuously differentiable. Then, in the region \mathcal{T} , x_g is a globally asymptotically stable equilibrium of f_θ^T if, $\forall t \in \mathbb{R}_{\geq 0}$:*

1. $d_t = d_{t+\Delta t}$, for $y_0 = y_g$,
2. $d_t > d_{t+\Delta t}$, $\forall y_0$ with $x_0 \in \mathcal{T} \setminus \{x_g\}$,

where $\Delta t \in \mathbb{R}_{>0}$.

Proof. To prove this theorem, we demonstrate that if the surrogate stability conditions are satisfied, then the stability conditions from Theo. 3 must also hold. This leads to x_g being a globally asymptotically stable equilibrium of f_θ^T .

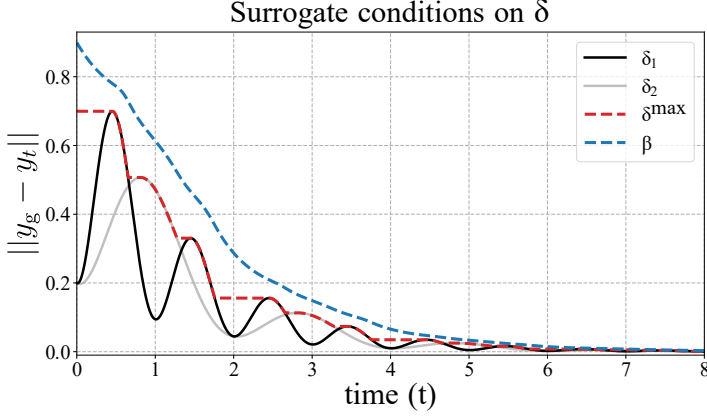


Figure 4: Time evolution of two functions δ , δ_1 and δ_2 , starting with different initial conditions y_0 , but same d_0 . Both satisfy the surrogate stability conditions for $\Delta t = 2$. Additionally, the values of δ^{\max} and β , computed using these functions, are shown. In this representation, $\delta = e^{-a \cdot t} (\sin^2(\omega t) + d_0 \cdot \cos^2(\omega t))$ with $a = 0.75$, $d_0 = 0.2$, and $\omega = [\pi, \pi/2]$.

a) *Second stability condition of Theo. 3*

Let us begin by analyzing the fulfillment of the second stability condition from Theo. 3. This condition states that only x_g can map to y_g via ψ_θ . Then, since y_g is defined as $\psi_\theta(x_g)$, we need to establish that no other x_t maps to y_g . To achieve this, we must note that both x_t and x_0 belong to the same state space \mathcal{T} . Therefore, showing that this statement holds $\forall x_0 \in \mathcal{T}$ implies that it also holds $\forall x_t \in \mathcal{T}$.

Now, assume, for the sake of contradiction, that there exists some x_0 such that $x_0 \neq x_g$ and $y_0 = \psi_\theta(x_0) = y_g$. Also assume that the surrogate conditions 1 and 2 hold. Then, according to condition 2, $y_t \neq y_{t+\Delta t}$, which contradicts condition 1. Consequently, the second stability condition must be satisfied.

b) *First stability condition Theo. 3*

Let us now study the first stability condition. Our goal is to prove that y_g is a globally asymptotically stable equilibrium of $f_\theta^{\mathcal{T} \rightarrow \mathcal{L}}$ within the region \mathcal{L} . Surrogate condition 2 hints that the system's stability might be verified using a Lyapunov candidate defined as a function of d_t . This is because the condition enforces the distance d_t to strictly decrease within the interval defined by Δt . However, this does not necessarily imply that the Lyapunov candidate consistently strictly decreases with time, as it is possible for it to strictly increase locally while adhering to this condition, as illustrated in Fig. 4. Therefore, we propose to demonstrate the global asymptotic stability of y_g using Theo. 2. Specifically, we aim to do so by employing a class- \mathcal{KL} upper bound β that fulfills (3).

To achieve this, we first define an evolution function for the distance d_t , for a given y_0 and t , as $\delta : \mathcal{L} \times \mathbb{R}_{\geq 0} \rightarrow \mathbb{R}_{\geq 0}$, with $\delta(y_0, t) = \|y_g - \Phi_\theta^y(t, y_0)\|$. Here, Φ_θ^y represents the evolution function of y_t under the dynamical system $f_\theta^{\mathcal{T} \rightarrow \mathcal{L}}$. Then, we can express the upper bound condition of β as

$$\delta(y_0, t) \leq \beta(d_0, t),$$

where $d_0 = \delta(y_0, 0)$. Recall that for ensuring asymptotic stability, β must also satisfy the following properties: i) $\beta(0, t) = 0$,

ii) β weakly decreases with t , iii) β is continuous with respect to d_0 and t , iv) $\beta \rightarrow 0$ as $t \rightarrow \infty$, and v) β strictly increases with d_0 .

It is important to note that verifying all these properties for a given β can lead to a lengthy proof. Thus, while we introduce β and discuss the key concepts behind its design here, the complete proof and details are provided in Prop. 1, Appendix A.

We now proceed to describe the three main aspects considered in the design of β .

- i) *Upper bound in time:* First, we need to identify an upper bound that weakly decreases with time. For this purpose, we introduce a function that computes the maximum of δ over the window $[t, t + \Delta t]$ for any given y_0 and t , i.e.,

$$\delta_{t+\Delta t}^{\max}(y_0, t) = \max_{s \in [t, t+\Delta t]} \delta(y_0, s).$$

Clearly, this function serves as an upper bound for δ . Moreover, this function must weakly decrease with time. Considering surrogate condition 2, which indicates that $\forall s \in [t, t + \Delta t]$, we have $\delta(y_0, s + \Delta t) < \delta(y_0, s)$, it follows that there is no δ greater than $\delta_{t+\Delta t}^{\max}$ in the interval $[t + \Delta t, t + 2\Delta t]$. By recursively extending this observation for every interval $[t + n \cdot \Delta t, t + (n + 1) \cdot \Delta t]$, with $n \in \mathbb{N}$, we can conclude that $\delta_{t+\Delta t}^{\max}$ weakly decreases with time.

- ii) *Upper bound in space:* The function $\delta_{t+\Delta t}^{\max}(y_0, t)$ provides an upper bound of δ for a given y_0 . However, $\beta(d_0, t)$ depends on d_0 rather than directly on y_0 . To address this, for any specified d_0 , we must ensure that $\beta \geq \delta$ for every y_0 located at this particular distance from the equilibrium. The set of y_0 fulfilling this condition can be defined as $\mathcal{V}_0(d_0) = \{y_0 \in \mathcal{L} : \|y_g - y_0\| = d_0\}$. Taking this into account, we can then introduce the following upper bound that depends on d_0 :

$$\delta^{\max}(d_0, t) = \max_{y_0 \in \mathcal{V}_0(d_0)} (\delta_{t+\Delta t}^{\max}(y_0, t)).$$

- iii) *Strictly increasing/decreasing function:* Similarly to $\delta_{t+\Delta t}^{\max}$, the function δ^{\max} also weakly decreases as a function of time (see Appendix A for details). This is not inherently problematic, as it verifies the properties of class- \mathcal{KL} functions. However, β must strictly increase as a function of d_0 , and, for this to be the case in our formulation, β must also strictly decrease as a function of time, $\forall d_0 \in \mathcal{L} \setminus \{y_g\}$.

To achieve this, we treat β as the evolution function of a first-order linear dynamical system with state z_t , using δ^{\max} as the reference. This leads to the equation

$$\dot{z}_t = \alpha(z_t - \delta^{\max}),$$

where $\alpha < 0$ and an initial condition z_0 greater than $\delta_0^{\max} = \delta^{\max}(d_0, 0)$ ensures that β strictly decreases with time and remains above δ^{\max} (and, consequently, above δ) for all $d_0 \in \mathcal{L} \setminus \{y_g\}$. By choosing $z_0 = \delta_0^{\max} + d_0$, β can then be expressed as

$$\beta(d_0, t) = z_0 + \int_0^t \dot{z}_s ds.$$

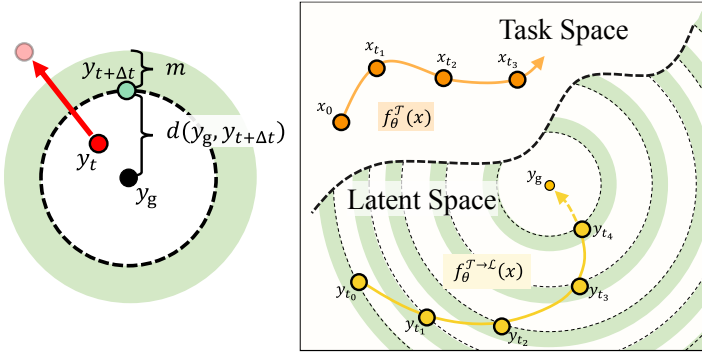


Figure 5: Left: Illustration of the effect of optimizing ℓ_{stable} in one triplet. Right: Example of trajectories generated with f_θ^T and $f_\theta^{T \rightarrow L}$ **post-training**. Each $y_{t+\Delta t}$ is closer to y_g than its predecessor y_t .

Based on Prop. 1, Appendix A, we can confirm that our formulation for β is a valid class- \mathcal{KL} upper bound of δ . This indicates that the second stability condition of Theo. 3 is satisfied, concluding our proof. \square \square

4.2.3 Loss Function

Notably, we can enforce the surrogate stability conditions from Theo. 4 within a DNN by minimizing the following expression $\forall y_0 \in \mathcal{L}$ and $\forall t \in \mathbb{R}_{\geq 0}$:

$$\max(0, m + d(y_g, y_{t+\Delta t}) - d(y_g, y_t)), \quad (5)$$

where $m \in \mathbb{R}_{>0}$. This function resembles the form of the triplet loss introduced in Sec. 3.4. In this context, y_g serves as the anchor sample, $y_{t+\Delta t}$ as the positive sample, and y_t as the negative sample. Let us explore how this expression induces the fulfillment of the surrogate stability conditions within a DNN.

a) Second surrogate condition

For any y_0 where $x_0 \neq x_g$, minimizing (5) enforces transitions to progressively approach y_g . This is achieved as it implies that

$$d(y_g, y_{t+\Delta t}) + m \leq d(y_g, y_t),$$

and, therefore, $d(y_g, y_{t+\Delta t}) < d(y_g, y_t)$, i.e., the second surrogate condition (see Fig. 5).

b) First surrogate condition

In contrast, the state x_g maps to y_g by construction, which modifies the behavior of (5) when $y_0 = y_g = \psi_\theta(x_g)$. In this case, for $t = 0$, the distance $d(y_g, y_0)$ cannot be modified through the parameters of the DNN, since it is zero by construction. Hence, the minimum of (5) is achieved at m , provided that $y_{0+\Delta t}$ also equals y_g . Moreover, under the same logic, for this initial condition, any $y_{t+\Delta t}$ gets modified towards the value of y_g . Consequently, the first surrogate condition is enforced.

Finally, since $\delta(y_0, t) = d(y_g, y_t)$, we present the stability loss function as

$$\ell_{\text{stable}} = \sum_{y_0 \in \mathcal{B}^s} \sum_{t \in \mathcal{H}^s} \max(0, m + \delta(y_0, t + \Delta t) - \delta(y_0, t)). \quad (6)$$

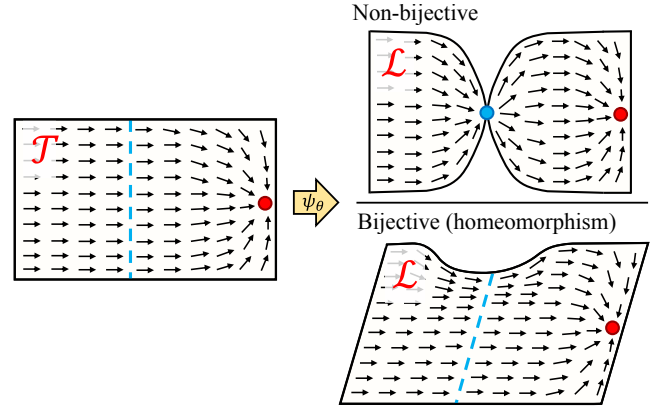


Figure 6: Non-bijective vs bijective solution. In the non-bijective case, every point on the blue line in \mathcal{T} maps to the blue point in \mathcal{L} . In the bijective case, the original line undergoes a transformation that both compresses and skews it, yet a one-to-one mapping is maintained.

In this equation, \mathcal{B}^s denotes a batch of initial latent states y_0 . These states are derived by mapping initial states x_0 (**sampled randomly** from \mathcal{T}) via the function ψ_θ . Meanwhile, \mathcal{H}^s represents a set of time points t at which the loss is minimized.

To compute this loss, we must recall that the evolution function of y_t is represented as Φ_θ^y . Consequently,

$$\delta(y_0, t) = \|y_g - \Phi_\theta^y(t, y_0)\|.$$

Given the absence of an analytical representation for Φ_θ^y , we approximate it using the forward Euler method, and optimize it using BPTT, in a similar manner to Sec. 4.1.

Importantly, optimizing this loss for all $t \in \mathbb{R}_{\geq 0}$ using BPTT is not feasible, as it would necessitate computing the loss over an infinite number of samples. Nevertheless, this limitation is not a significant concern when dealing with time-invariant dynamical systems. In such systems, any state y_t can be equivalently represented by an initial condition y_0 , since both reside in the same state space \mathcal{L} . Consequently, when states are randomly sampled from \mathcal{T} , and thereby from \mathcal{L} , we are essentially sampling from the space of all possible y_t .

4.3 On the Stability Loss Metric

Intentionally, we have not specified which distance function or metric should be used for computing the stability loss, since it should be selected depending on the geometry employed to describe the robot's state space.

To elaborate on this point, recall that the learned dynamical system can be expressed as $\dot{x}_t = \phi_\theta(y_t)$. It then follows that the output of our model is entirely determined by the latent state y_t . This implies that if two different states x_t^a and x_t^b map to the same latent state, that is, $y_t = \psi_\theta(x_t^a) = \psi_\theta(x_t^b)$, the time derivative computed by the learned dynamical systems for both states will be identical. Such behavior would manifest in certain states if ψ_θ were a non-bijective⁵ function.

⁵More rigorously, the property being described is that of non-injective functions. However, for practical purposes, we can define the codomain of ψ_θ to be equal to its image, which is the property that an injective function must have to be bijective. Hence, in this specific context, we use these terms interchangeably.

It would, therefore, be problematic if the learning process were to force ψ_θ to be non-bijective, as this would constrain the family of solutions to which the system can converge, harming the DNN's optimization process. Ideally, we would like ψ_θ to have the capacity to converge to a bijective function, such that every state x_t maps to a unique latent state y_t . Consequently, for any state x_t , it would be possible to compute a value of \dot{x}_t that is independent of those calculated for any other state. Fig. 6 presents an example of bijective and non-bijective mappings between dynamical systems.

It turns out that the capacity of ψ_θ to converge to a bijective function is closely linked to the metric used in calculating ℓ_{stable} , which should be chosen based on the geometry of the robot's state space. In the following subsection, we explore this relationship in more depth.

4.3.1 Homeomorphisms and State Space Geometry

To study under which conditions ψ_θ can converge to a bijective function, let us introduce the concept of *topologically equivalent* manifolds. Two manifolds, e.g., \mathcal{T} and \mathcal{L} , are topologically equivalent if a continuous and bijective mapping, known as a *homeomorphism*, exists between them [43]. In other words, two topologically equivalent manifolds can be *stretched*, *compressed*, or *twisted* into each other without *tearing* or *gluing* space. Since DNNs are continuous functions⁶, a bijective function ψ_θ would also serve as a homeomorphism⁷ between \mathcal{T} and \mathcal{L} .

Moreover, since we have a notion of distance in both \mathcal{T} and \mathcal{L} , it follows that these manifolds are metric spaces. A key property of metric spaces is that their topology is generated by their distance functions. Therefore, if two metric spaces are topologically equivalent, their metrics are termed as being *equivalent* [46]. It is important to clarify that this does not necessarily mean that the two distance functions are identical, but rather that they induce metric spaces that are homeomorphic to each other.

In our context, this implies that the distance function employed in the stability loss (6) must induce a topology in \mathcal{L} that is equivalent to that of \mathcal{T} . For example, if orientations are described using unit quaternions, the topology of \mathcal{T} would be spherical. Then, the stability loss metric should generate a topology that is homeomorphic to the sphere. Otherwise, it would be infeasible for the DNN to establish a homeomorphism between \mathcal{T} and \mathcal{L} . In Sec. 5, we utilize unit quaternions to represent orientations; for a detailed discussion on metrics and pose control in this context, the reader is referred to Appendix B.

4.4 Boundary Conditions

Lastly, it is crucial to ensure a dynamical system evolving in \mathcal{T} always remains within this manifold. Two scenarios are relevant for this work: 1) \mathcal{T} is not positively invariant with

⁶We can assume this since every broadly used model is continuous [44, 45].

⁷DNNs are commonly continuously differentiable, so, sometimes in the literature the term *diffeomorphism* is employed instead, as diffeomorphisms are continuously differentiable homeomorphisms.

respect to $f_\theta^\mathcal{T}$, and 2) Euclidean operations are employed in non-Euclidean state spaces.

4.4.1 Positively Invariant Sets

In PUMA, the stability of a motion is enforced by randomly sampling points from \mathcal{T} and minimizing ℓ_{stable} . Thus, stability cannot be ensured in regions where this loss is not minimized, i.e., outside of \mathcal{T} . When boundaries are imposed on the robot's workspace, the learned dynamical system $f_\theta^\mathcal{T}$ can potentially evolve towards these boundaries, leaving \mathcal{T} . Hence, to ensure stability, a state evolving within \mathcal{T} must not leave \mathcal{T} . In other words, \mathcal{T} has to be a *positively invariant set* with respect to $f_\theta^\mathcal{T}$ [6, 41].

To address this scenario, we design the dynamical system so that it cannot leave \mathcal{T} by construction. This can be achieved by projecting any transitions that would leave \mathcal{T} back onto its boundary. For example, in Euclidean state spaces, \mathcal{T} can be represented as a hypercube; therefore, in this case, this projection is achieved by saturating/clipping the points that would leave \mathcal{T} . Furthermore, we have found that introducing an additional loss, denoted as ℓ_∂ , for optimizing the DNN can aid the optimization process. As proposed in [6], this can be accomplished by calculating the scalar product between the dynamical system's velocity $v(x_t)$ (which equates to $f_\theta^\mathcal{T}$ for first-order systems) and the outward-pointing normal vector $n(x_t)$ at states within the boundary of \mathcal{T} . This product should be ensured to be equal to or less than zero. For DNNs, this can be achieved by minimizing

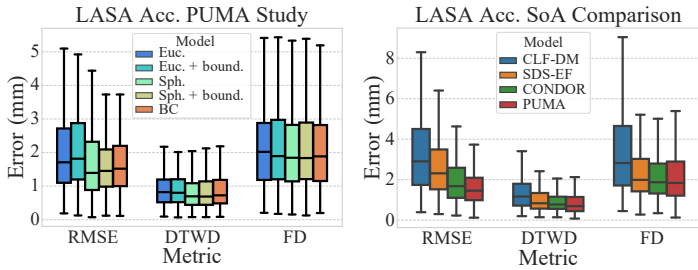
$$\ell_\partial = \max(0, n(x_t) \cdot v(x_t)).$$

4.4.2 Non-Euclidean State Spaces

When modeling dynamical systems in non-Euclidean state spaces, it is crucial to ensure that states do not evolve outside the manifold representing them. For instance, unit quaternions must remain within the unit sphere. However, if these states are evolved using Euclidean geometry tools, such as the forward Euler integration method, deviations from the manifold are likely to occur.

Non-Euclidean state spaces are commonly defined within a higher-dimensional Euclidean space and can sometimes be constructed by incorporating constraints into this space. Consider the unit quaternion as an example; its state space consists of every vector in \mathbb{R}^4 with a unit norm, forming the 3-sphere \mathcal{S}^3 . Hence, in such scenarios, by incorporating an operation that enforces these constraints, such as normalization for \mathcal{S}^3 , into the structure of the DNN representing $f_\theta^\mathcal{T}$, we ensure that transitions remain within the manifold. Moreover, in this way, the distortions that this operation introduces into the dynamical system's output are factored into the DNN's optimization process, ensuring they are accounted for.

Alternatively, when we have access to the *Riemannian metric* of a state space manifold, it is possible to use the *exponential* and *logarithmic maps* to do Euclidean calculus in the *tangent bundle* of the manifold, and map the solution back on the manifold (the reader is referred to [47] for more details).



(a) Comparison of different variations of PUMA. (b) Comparison of PUMA with other state-of-the-art (SoA) methods.

Figure 7: Accuracy study in the LASA dataset.

5 Experiments

We validate our method with three datasets, each allowing us to study different aspects of it. For evaluation purposes, we use these datasets under the assumption of perfect tracking of the desired state derivatives, \dot{x}_t^d , provided by f_θ^T , without any involvement of robots in this process. Subsequently, we test our method in two real-world settings using two different robots. Details on the DNN’s hyperparameters optimization process are presented in Appendix C.

5.1 Euclidean Datasets

Firstly, we evaluate our method using datasets of Euclidean motions. This enables us to study how different variations of PUMA perform for Euclidean motions and compare the performance of PUMA against state-of-the-art methods for stable Euclidean motion generation.

5.1.1 LASA

The LASA dataset [4] is composed of 30 human handwriting motions, each consisting of 7 demonstrations of desired trajectories under different initial conditions. These demonstrations are two-dimensional and designed to be modeled using first-order systems, i.e., output desired velocities as a function of their positions. To compare accuracy performance between different models, we employ the same metrics in every experiment: 1) Root Mean Squared Error (RMSE), Dynamic Time Warping Distance (DTWD) [48] and Fréchet Distance (FD) [49].

a) Accuracy

Fig. 7a showcases the accuracy of four variations of PUMA. Here, we compare how different distance metrics in ℓ_{stable} perform for motions in Euclidean spaces, specifically the Euclidean distance and the great-circle (spherical) distance. Furthermore, we also examine the influence of ℓ_∂ on the accuracy of the learned motions. We use Behavioral Cloning (BC) without a stability loss as a performance upper bound for comparison. Interestingly, each variation of PUMA achieves a similar performance; however, PUMA with a spherical metric shows slightly better performance than PUMA with an Euclidean metric. This suggests that the DNN has no difficulties in mapping the

Table 1: Percentage of unsuccessful trajectories over the LASA dataset ($L = 2500$, $P = 2500$, $\epsilon = 1\text{mm}$).

Behavioral Cloning	PUMA (Euc.)	PUMA (Euc. + ℓ_∂)	PUMA (Sph.)	PUMA (Sph. + ℓ_∂)
36.4653%	0.0000%	0.0000%	0.0000%	0.0000%

Euclidean space \mathcal{T} into a spherical space \mathcal{L} . Lastly, we can also observe that the use of ℓ_∂ does not harm the accuracy performance of PUMA.

b) Stability

The stability of the motions learned by PUMA hinges on the successful minimization of (4), which we need to empirically test after the learning process concludes. To do this, we integrate the dynamical system over L time steps, starting from P initial states, and observe whether the system converges to the goal. The larger the P , the more accurate our results. If L is sufficiently large, the system should reach the goal after L steps. By measuring the distance between the last state visited and the goal, and confirming that it falls below a pre-set threshold ϵ , we can evaluate if a trajectory is successful (i.e., it converges to the goal).

Table 1 provides the stability results of BC and different PUMA variations. The data shows that every variation of PUMA successfully enforces stability across the dataset, generating no unsuccessful trajectories. When compared to BC, which has a 36.4653% rate of unsuccessful trajectories, the benefit of the proposed loss in enforcing stability becomes clear.

c) State-of-the-art comparison

Fig. 7b presents an accuracy comparison of PUMA with other state-of-the-art methods, namely: 1) Control Lyapunov Function-based Dynamic Movements (CLF-DM) using Gaussian Mixture Regression (GMR) [5], 2) Stable Dynamical System learning using Euclideanizing Flows (SDS-EF) [2], and 3) CONDOR. The results for PUMA correspond to the best-performing variation in this dataset, i.e., spherical distance with ℓ_∂ . We observe that PUMA achieves competitive results, demonstrating similar performance in DTWD and FD to CONDOR and SDS-EF, and slightly superior performance under RMSE.

d) Boundary loss

Fig. 8 demonstrates the effect of the boundary loss ℓ_∂ in PUMA. Figures 8a and 8b present an example of the qualitative performance of PUMA and CONDOR when no boundary loss is applied. In the top-left region of these images, PUMA exhibits non-smooth trajectories at the boundary, which abruptly change direction due to the applied saturation (see Sec. 4.4). Conversely, CONDOR learns a smoother trajectory in this region. This feature in PUMA disappears when ℓ_∂ is employed, as depicted in Fig. 8c. Finally, Fig. 8d provides a quantitative evaluation of the boundary loss, confirming our qualitative observations.

In the context of this work, this loss is **only relevant for Euclidean state spaces**. This is because we do not introduce boundaries in the state space when controlling orientation in \mathcal{S}^3 .

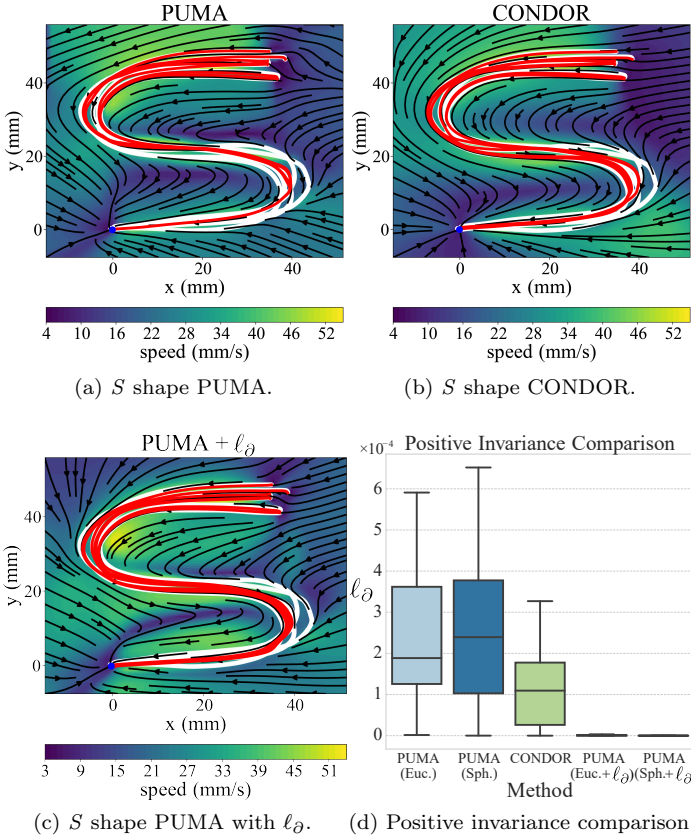


Figure 8: Positive invariance evaluation. In figures (a)-(c) white curves represent demonstrations. Red curves represent learned motions when starting from the same initial conditions as the demonstrations. The arrows indicate the vector field of the learned dynamical system.

5.1.2 LAIR

Contrary to the LASA dataset, the LAIR dataset [9] is specifically designed to evaluate second-order motions, i.e., those that map current position and velocity to acceleration. This dataset comprises 10 human handwriting motions, with the state being 4-dimensional, encompassing a 2-dimensional position and velocity. The dataset’s shapes contain multiple position intersections, intentionally designed to necessitate the use of at least second-order systems for their modeling.

a) CONDOR / PUMA comparison

The state-of-the-art methods outlined in Sec. 5.1.1, excluding CONDOR, do not address the problem of learning stable second-order systems. This can be attributed to the increased difficulty inherent in learning such systems compared to first-order systems. As a result, we compare the performance of PUMA with that of CONDOR. Fig. 9a illustrates the comparative accuracy of both methods, with PUMA surpassing CONDOR on all metrics. PUMA’s greater learning flexibility allows it to converge to solutions beyond CONDOR’s capabilities. Moreover, this enhanced flexibility, as depicted in Fig. 9b, endows PUMA with a more stable learning process. This is crucial, as motions with unsuccessful trajectories must be discarded. Therefore, if the learned dynamical system is

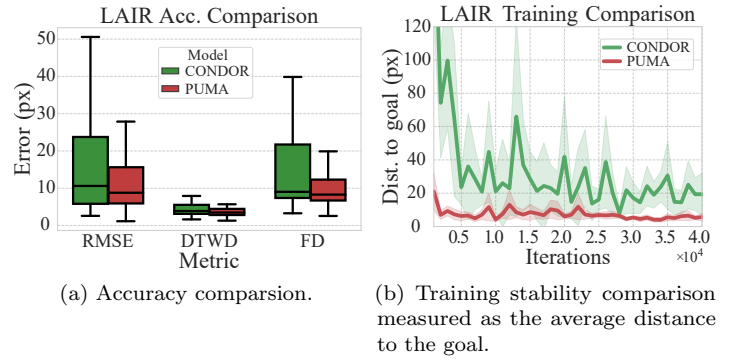


Figure 9: LAIR dataset PUMA / CONDOR comparison.

Table 2: Percentage of unsuccessful trajectories over the LAIR dataset ($L = 2500$, $P = 2500$, $\epsilon = 10\text{px}$).

Behavioral Cloning	PUMA (Euc.)	PUMA (Euc. + ℓ_∂)	PUMA (Sph.)	PUMA (Euc. + ℓ_∂)
14.1160%	0.0000%	0.0000%	0.0000%	0.0000%

evaluated multiple times throughout a learning process, more learning stability yields a larger set of motions without unsuccessful trajectories, thus offering more alternatives to select from.

b) Stability

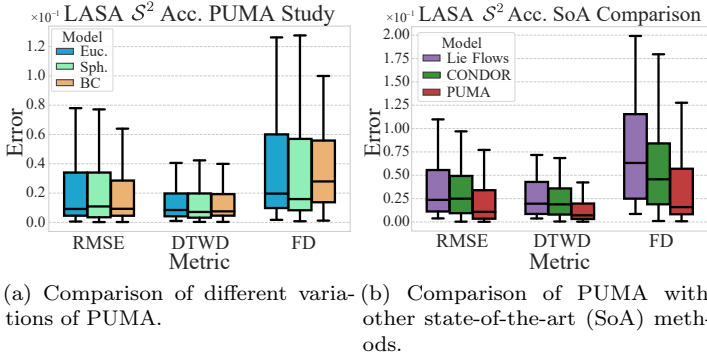
Table 2 presents the results of stability analysis for PUMA on the LAIR dataset. Similar to the findings with the LASA dataset, every variation of PUMA achieves a 0% rate of unsuccessful trajectories. This validates PUMA’s ability to learn stable second-order motions.

5.2 Non-Euclidean dataset: LASA \mathcal{S}^2

The LASA \mathcal{S}^2 dataset [11] comprises 24 motions, each with 3 demonstrations, selected from the LASA dataset. Unlike the LASA dataset, the LASA \mathcal{S}^2 dataset represents these motions in spherical geometry, as indicated by its name, in \mathcal{S}^2 . The sphere, where the motions evolve, is structured similarly to unit quaternions, though with one less dimension. Essentially, we have a 3-dimensional Euclidean space where vectors are constrained to have unit norm. As a result, the state space is a 2-dimensional spherical manifold embedded in this 3-dimensional space. This setup allows us to examine the performance of PUMA in a manifold with similar attributes to that of unit quaternions. However, the simpler visualization of this setup facilitates a more intuitive analysis of PUMA’s performance.

5.2.1 Accuracy

Fig. 10a presents the performance of two variations of PUMA, namely with Euclidean and spherical distance functions. Moreover, BC is included, serving as an upper-bound reference. As explained in Sec. 5.1.1, the boundary loss ℓ_∂ does not apply in this case; hence, it is not evaluated. We can observe that the accuracy performance of both variations of

Figure 10: Accuracy study in LASA \mathcal{S}^2 dataset.Table 3: Percentage of unsuccessful trajectories over the LASA \mathcal{S}^2 dataset ($L = 2500$, $P = 2500$, $\epsilon = 0.06$).

Behavioral Cloning	CONDOR	PUMA (Euc.)	PUMA (Sph.)
15.9217%	7.3133%	0.0000%	0.0000%

PUMA is very similar, and BC performs slightly better than both of them.

5.2.2 Stability

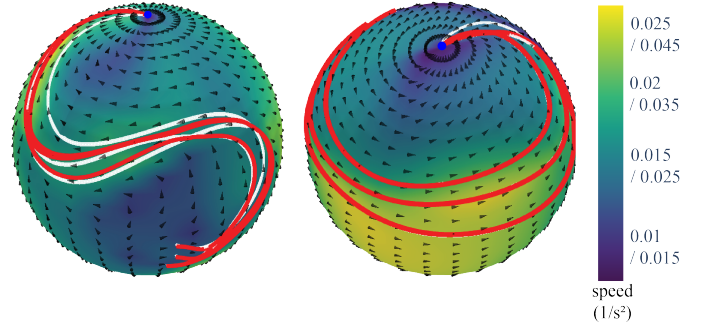
Table 3 depicts the stability results for the LASA \mathcal{S}^2 dataset. In this case, we also conducted a stability analysis of CONDOR, as our discussion in Sec. ?? suggested that this method should not be capable of ensuring stability in non-Euclidean state spaces. This assertion is confirmed by the data in Tab. 3, which shows that CONDOR yields 7.3133% of unsuccessful trajectories. When compared to BC, which has a 15.9217% rate of unsuccessful trajectories, it can be inferred that CONDOR reduces the number of unsuccessful trajectories in non-Euclidean state spaces. However, its performance is still far from satisfactory. In contrast, both versions of PUMA achieve 0% of unsuccessful trajectories, marking a significant improvement. Moreover, it validates that the Euclidean distance is effective for enforcing stability in spheres, as it can induce spherical metrics, such as the chordal distance, in lower-dimensional manifolds.

5.2.3 Qualitative Analysis

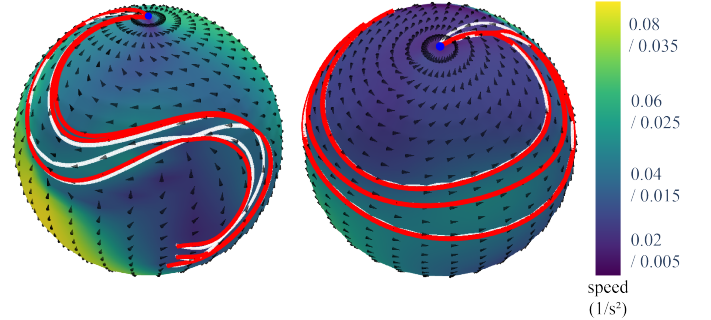
Fig. 11 illustrates the motions learned with PUMA in \mathcal{S}^2 , using both spherical and Euclidean distance. Within the observed region of the sphere, the vector field exhibits no spurious attractors. Furthermore, when initiated from the same conditions as the demonstrations, the trajectories in both cases show an accurate reproduction of the motions.

5.2.4 State-of-the-art Comparison

Fig. 10b depicts a comparison between three methods: 1) CONDOR, 2) PUMA, and 3) a method developed for



(a) Results using the great-circle distance.



(b) Results using the Euclidean (chordal) distance.

Figure 11: Motions learned with PUMA in \mathcal{S}^2 . White curves represent demonstrations. Red curves represent learned motions when starting from the same initial conditions as the demonstrations. The arrows indicate the vector field of the learned dynamical system.

learning stable motions in non-Euclidean manifolds using tools from Lie Theory, which we will refer to as *Lie Flows* [11]. PUMA outperforms both CONDOR and Lie Flows in terms of accuracy. Moreover, in contrast to CONDOR, PUMA also successfully ensured stability in this dataset. This clearly shows PUMA’s superiority over CONDOR in non-Euclidean state spaces.

5.3 Real-world Experiments

We validate our method in two real-world setups, using two different robots. Both robots have six degrees of freedom, with their end-effector pose represented in $\mathbb{R}^3 \times \mathcal{S}^3$ and controlled using PUMA. In these experiments, f_{θ}^T is employed to generate velocity references in real time, which are then sent to the low-level controllers responsible for tracking these references in the robots. Note that throughout the experiments, we operated under the assumption that the target states of the robots are already known.

5.3.1 Greenhouse

This experiment was conducted in a greenhouse, where a robot was trained to reach a black marker on a tomato plant (see Fig. 12). This marker, simulating a plant’s peduncle, represented the target state the robot must reach to harvest the plant. Utilizing the marker in this experiment allowed us to test the method without causing harm to the plant. This task

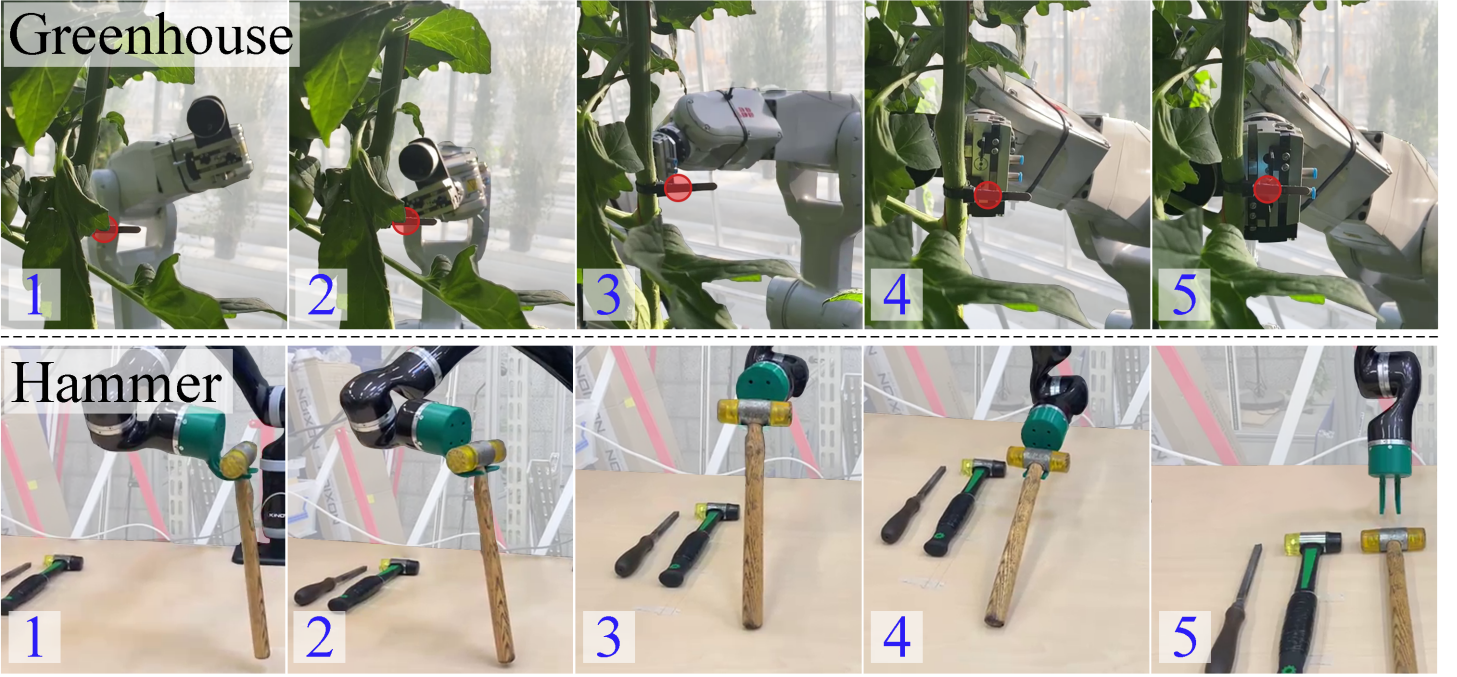


Figure 12: Two sequences of frames, each depicting a robot performing a task: 1) operating in a greenhouse, and 2) placing a hammer. The red circle is used to highlight a target marker in the greenhouse experiment.

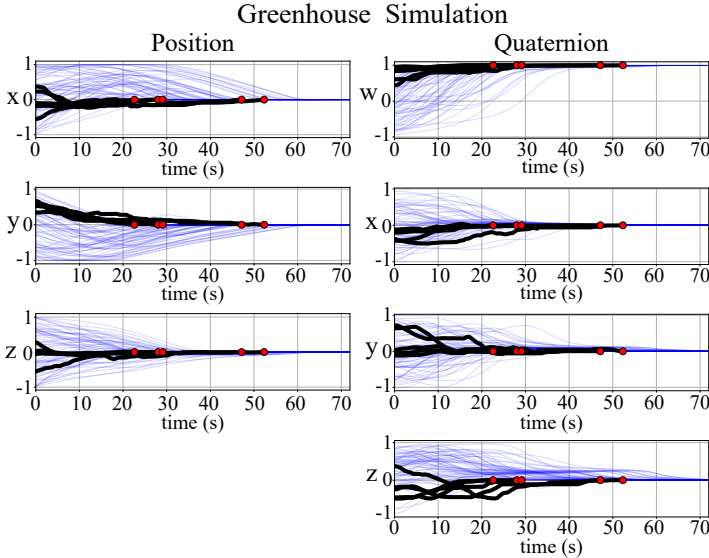


Figure 13: Simulated trajectories, as a function of time, of the greenhouse experiment. Blue trajectories correspond to evaluations of the model under different initial conditions and the black trajectory corresponds to the demonstration. The red point is the goal.

presents significant challenges, as it requires the robot to perform precise position and orientation control while considering the plant’s complex geometry, which is non-trivial to model. In a practical setting, a motion library should be developed to account for the unique characteristics of individual plants and targets. This library could then be used to select or combine suitable motions to create an appropriate movement strategy that considers these factors. This experiment represents a preliminary step towards achieving this objective.

In this experiment, we utilized an *ABB IRB 1200* robot, which can be equipped with the *Externally Guided Motion*⁸ module, allowing real-time joint velocity control. As the motion takes place in the end-effector space, the desired velocity at each time step was calculated using f_{θ}^T , and subsequently mapped to the joint space. This conversion was accomplished using the inverse kinematics module with joint limits from the *Robotics Toolbox* [50]. Similarly, we translated the robot’s estimated joint state into the end-effector space using the forward kinematics module from the same toolbox. The same approach was taken to collect the demonstrations of this task directly in the end-effector space, where a space mouse was employed to teleoperate the robot.

Fig. 13 presents the demonstrations and simulations of motions conducted in this experiment. It can be observed that five demonstrations were provided. Note that these demonstrations do not need to have the same end time; only the final state needs to be consistent. Over a span of 70 seconds, all simulated trajectories visibly converge to the goal. For more details, the reader is referred to the attached video.

5.3.2 Hammer

The second experiment involves a robot accurately positioning a hammer next to other tools on a table. This task requires precise control of the robot’s position and orientation, as shown in Fig. 12. We are interested in controlling the hammer’s movement, so we assume that the state of the hammer directly relates to the state of the robot’s end effector. This assumption is necessary because the employed low-level controller acts on the robot’s end-effector state, and we ensure stability in this state space. Given that the hammer is

⁸Code: https://github.com/ros-industrial/abb_robot_driver.

attached to the robot through a double hook, this assumption is valid as long as the hammer’s head is securely held. This assumption breaks down towards the end of the motion when the robot places the hammer on the table. However, since the final states of both the hammer and the robot are close, we observed that ensuring stability in the end-effector’s motion effectively guides the hammer’s motion towards its goal state, as can be seen in Fig. 12 and the attached video.

We used the *Kinova Gen2 Ultra lightweight robot* arm with a double hook replacing its default gripper. The control commands obtained from f_θ^T were directly sent to a Cartesian space controller from Kinova⁹. The demonstrations were collected through kinesthetic teaching, i.e., physically moving the robot along desired paths while having the robot in gravity compensation mode. The simulated performance in this task was similar to that in the greenhouse, given that the state space was identical in both cases. We refer the reader to the attached video for examples of the robot executing this task from various initial conditions.

6 Conclusions

We introduced a novel approach for learning stable robotic motions in both Euclidean and non-Euclidean state spaces. To achieve this, we introduced a new loss function based on the triplet loss from the deep metric learning literature. We validated this loss both theoretically and experimentally.

Our approach, PUMA, showcased state-of-the-art performance in every experiment, both in terms of accuracy and stability. It was validated using datasets where the dynamical system evolution was simulated, as well as real robotic platforms where it was employed to provide control commands to low-level controllers.

Compared to previous work, PUMA offers not only an improvement in addressing non-Euclidean state spaces but also increased flexibility by reducing restrictions in the latent space of the DNN, leading to generally better performance. More specifically, in previous work, the latent dynamical system is constrained to evolve along straight lines towards the goal. In contrast, PUMA allows the latent dynamical system to converge towards a broader range of stable dynamical systems, since its loss function only enforces the latent dynamical system to reduce the distance towards the goal. This feature expands the set of feasible solutions available to the DNN during optimization, thereby enhancing the model’s adaptability.

Lastly, while this paper’s findings are promising, there are also limitations that can be addressed in future works. Firstly, further exploration of the scalability properties of PUMA is needed, as the largest state space employed in this paper had 7 dimensions. Secondly, we have so far focused on learning independent motion primitives for specific tasks. A relevant line of research would be integrating this model into a larger framework where multiple primitives are learned and combined together. Finally, another interesting research direction is studying the integration of these approaches with the low-level control of the robots. Currently, it is assumed that the transitions requested by PUMA can be tracked by the

controllers of the robot. However, this is not always the case, and it would be beneficial to incorporate this information into the learning framework.

Acknowledgements

The authors would like to thank Xin Wang, Thomas Versmissen, Bastiaan Vroegindeweij, Rekha Raja, Gert Kootstra, and Eldert van Henten of the Agricultural Biosystems Engineering Group at Wageningen University and Research. Their assistance during the real-world experiments of this work, conducted at their facilities, was invaluable.

Funding

This research is funded by the Netherlands Organization for Scientific Research project Cognitive Robots for Flexible Agro-Food Technology, grant P17-01, and by the NXTGEN national program.

Appendix

A Upper Bound β

In this section, we introduce and prove the proposition used in Sec. 4.2.2 to demonstrate that the surrogate stability conditions ensure asymptotic stability in the dynamical system $f_\theta^T(x_t)$.

Proposition 1 (Existence of class- \mathcal{KL} function). *Consider a dynamical system $\dot{y}_t = f(y_t)$ with $f : \mathcal{L} \subset \mathbb{R}^n \rightarrow \mathbb{R}^n$ continuously differentiable, and $\Phi_\theta^y(t, y_0) : \mathbb{R}_{\geq 0} \times \mathcal{L} \rightarrow \mathcal{L}$ as its evolution function. For a distance function d_t in \mathcal{L} , we define its evolution, for a given t and y_0 , as $\delta : \mathcal{L} \times \mathbb{R}_{\geq 0} \rightarrow \mathbb{R}_{\geq 0}$, with $\delta(y_0, t) = \|y_g - \Phi_\theta^y(t, y_0)\|$.*

Then, consider the function $\beta : \mathbb{R}_{\geq 0} \times \mathbb{R}_{\geq 0} \rightarrow \mathbb{R}_{\geq 0}$ defined as

$$\beta(d_0, t) = z_0 + \int_0^t \dot{z}_s ds, \quad (7)$$

with derivative

$$\dot{z}_t = \alpha(z_t - \delta^{max}(d_0, t)), \quad (8)$$

where $\alpha \in \mathbb{R}_{<0}$ and

$$\delta^{max}(d_0, t) = \max_{y_0 \in \mathcal{Y}_0} \left(\max_{s \in [t, t+\Delta t]} \delta(y_0, s) \right), \quad (9)$$

with $\mathcal{Y}_0(d_0) = \{y_0 \in \mathcal{L} : \|y_g - y_0\| = d_0\}$ and $\Delta t \in \mathbb{R}_{>0}$. The initial condition z_0 is set as

$$z_0 = \delta_0^{max} + d_0, \quad (10)$$

where $\delta_0^{max} = \delta^{max}(d_0, 0)$.

Then, under the conditions of Theo. 4, i.e., $\forall t \in \mathbb{R}_{\geq 0}$,

1. $d_t = d_{t+\Delta t}$, for $y_0 = y_g$,
2. $d_t > d_{t+\Delta t}$, $\forall y_0 \in \mathcal{L} \setminus \{y_g\}$,

⁹Kinova’s controllers: <https://github.com/Kinovarobotics/kinova-ros>

Lemma 3 ($\beta > \delta$ and strictly decreasing). $\beta(d_0, t) > \delta(y_0, t)$ and $\beta(d_0, t)$ strictly decreases with respect to t , $\forall d_0 \in \mathbb{R}_{\geq 0} \setminus \{0\}$, $\forall t \in \mathbb{R}_{\geq 0}$, if:

1. δ^{\max} decreases with respect to t , $\forall d_0 \in \mathbb{R}_{\geq 0} \setminus \{0\}$.

Proof. Although δ^{\max} evolves as a function of time, we can infer from (8) that, locally, β behaves as a linear first-order dynamical system, with the origin at δ^{\max} . Given that $\alpha < 0$, it follows that β will converge towards δ^{\max} over time.

Moreover, (10) indicates that $z_0 > \delta_0^{\max}$ for every $d_0 > 0$. Given the properties of linear first-order systems, β will strictly decrease towards δ_0^{\max} , without ever reaching or overshooting this value. Combined with condition 1, which indicates that δ^{\max} decreases with respect to t for all $d_0 \in \mathbb{R}_{\geq 0} \setminus \{0\}$, we can conclude that β will always be greater than δ^{\max} and will continue to strictly decrease towards this value as a function of time. Therefore, $\beta > \delta$ and β strictly decreases with respect to t , $\forall d_0 \in \mathbb{R}_{\geq 0} \setminus \{0\}$. \square

Lemma 4 (δ^{\max} decreases over time). $\delta^{\max}(d_0, t)$ decreases with respect to t , $\forall d_0 \in \mathbb{R}_{\geq 0} \setminus \{0\}$, $\forall t \in \mathbb{R}_{\geq 0}$, if:

1. $d_t > d_{t+\Delta t}$, $\forall t \in \mathbb{R}_{\geq 0}$, $\forall y_0 \in \mathcal{L} \setminus \{y_g\}$, (Theo. 4, 2).

Proof. Let us define

$$\delta_{t+\Delta t}^{\max}(y_0, t) = \max_{s \in [t, t+\Delta t]} \delta(y_0, s), \quad (11)$$

which allows us to write $\delta^{\max} = \max_{y_0 \in \mathcal{Y}_0} (\delta_{t+\Delta t}^{\max})$. We will first prove that $\delta_{t+\Delta t}^{\max}$ decreases with t .

To do so, observe that condition 1 can be rewritten as $\delta(y_0, t + \Delta t) < \delta(y_0, t)$. Given that this condition holds true for every s in the interval $[t, t + \Delta t]$, none of the values of $\delta(y_0, s)$ computed in this interval can exceed the maximum of this interval, i.e., $\delta_{t+\Delta t}^{\max}(y_0, t)$, after Δt seconds. If there were such a value $\delta(y_0, s)$ that is greater than $\delta_{t+\Delta t}^{\max}(y_0, t)$ after Δt seconds, it would imply that $\delta(y_0, s)$ had increased, for some s , after Δt , contradicting condition 1. Therefore, $\delta_{t+\Delta t}^{\max}$ can only decrease as time progresses. Since this holds for all instances of t , we conclude that $\delta_{t+\Delta t}^{\max}$ decreases with respect to t , $\forall y_0 \in \mathcal{L} \setminus \{y_g\}$.

Now, the function δ^{\max} computes the maximum over a set of functions $\delta_{t+\Delta t}^{\max}$ with different initial conditions $y_0 \in \mathcal{Y}_0(d_0)$. However, for any given d_0 , $\forall y_0 \in \mathcal{L} \setminus \{y_g\}$, each one of these functions decreases with respect to time. Then, for any given interval of time, we have two possible scenarios:

- i) δ^{\max} is equal to one function $\delta_{t+\Delta t}^{\max}$ (the current maximum). In this case, δ^{\max} decreases with time, since $\delta_{t+\Delta t}^{\max}$ decreases with time.
- ii) The function that is currently the maximum over the set of functions $\delta_{t+\Delta t}^{\max}$ reaches a point in time t' where it changes. At the point where the change occurs, the function will be lower than or equal to its previous values for $t < t'$, since the previous maximum is decreasing. Furthermore, it will be greater than or equal to the values for $t > t'$, since the new maximum also decreases.

Therefore, we can conclude that $\forall d_0$ where $y_0 \in \mathcal{Y}_0(d_0)$ is not y_g , δ^{\max} decreases with respect to time. Moreover, by noting

that $\forall y_0 \in \mathcal{Y}_0(d_0)$, $d_0 \neq 0$ implies that $y_0 \neq y_g$, it follows that δ^{\max} decreases with respect to time, $\forall d_0 \in \mathbb{R}_{\geq 0} \setminus \{0\}$, $\forall t \in \mathbb{R}_{\geq 0}$. \square

As a consequence, the assumptions and conditions outlined in Prop. 1 enable us to apply Lemma 4 to demonstrate that the conditions of Lemma 3 are satisfied. This, in turn, leads us to the conclusion that $\beta > \delta$ and $\beta(d_0, t)$ strictly decreases with respect to t , $\forall d_0 \in \mathbb{R}_{\geq 0} \setminus \{0\}$, $\forall t \in \mathbb{R}_{\geq 0}$. Lastly, before we showed that, for $d_0 = 0$, $\beta(0, t) = 0$, $\forall t \in \mathbb{R}_{\geq 0}$. Therefore, in general, we have that $\beta \geq \delta$ and β decreases with respect to t , $\forall d_0 \in \mathbb{R}_{\geq 0}$, $\forall t \in \mathbb{R}_{\geq 0}$.

c) Continuity of β

We require β to be continuous with respect to t , for each fixed d_0 , and with respect to d_0 , for each fixed t . To achieve this, we will introduce Lemmas 5, 6 and 7.

Lemma 5. [Continuity of δ] If $\dot{y}_t = f(y_t)$ is continuously differentiable, then $\delta(y_0, t)$ is continuous with respect to y_0 and t .

Proof. Given that $\dot{y}_t = f(y_t)$ is continuously differentiable, it follows that $\Phi_\theta^y(t, y_0)$ is continuously differentiable with respect to both t and y_0 [51]. Moreover, since δ is a metric on \mathcal{L} defined by $\delta = ||y_g - \Phi_\theta^y(t, y_0)||$, it is continuous with respect to $\Phi_\theta^y(t, y_0)$ [52]. Since $\Phi_\theta^y(t, y_0)$ is continuously differentiable and thus continuous, and the composition of two continuous functions is continuous, it follows that $\delta(y_0, t)$ is continuous with respect to both y_0 and t . \square

Lemma 6 (δ^{\max} continuous with respect to t). δ^{\max} is a continuous function with respect to t , if δ is continuous with respect to t .

Proof. We will first prove this for $\delta_{t+\Delta t}^{\max}$ (as defined in (11)). Given that $\delta_{t+\Delta t}^{\max}$ is the maximum value of $\delta(y_0, s)$ over the interval $[t, t + \Delta t]$, any change in $\delta_{t+\Delta t}^{\max}$ must be due to a change in δ for some s in the boundaries of $[t, t + \Delta t]$. Then, since δ changes continuously, $\delta_{t+\Delta t}^{\max}$ can only change continuously as well. Thus, $\delta_{t+\Delta t}^{\max}$ is continuous with respect to t .

However, we need to show that $\delta^{\max} = \max_{y_0 \in \mathcal{Y}_0} (\delta_{t+\Delta t}^{\max})$ is continuous with respect to t . This follows from the fact that δ^{\max} computes the point-wise maximum along t over a set of continuous functions $\delta_{t+\Delta t}^{\max}$, which results in a continuous function [53]. \square

Lemma 7 (δ^{\max} continuous with respect to d_0). δ^{\max} is continuous with respect to d_0 , if δ is continuous with respect to y_0 .

Proof. Given the continuity of the function $\delta(y_0, t)$ with respect to y_0 , the function $\delta_{t+\Delta t}^{\max}$ computes the point-wise maximum along y_0 over a set of continuous functions, specifically $\{\delta(y_0, s) : s \in [t, t + \Delta t]\}$. Consequently, $\delta_{t+\Delta t}^{\max}$ is also continuous in y_0 [53].

Building on this, we seek to demonstrate that $\delta^{\max} = \max_{y_0 \in \mathcal{Y}_0} (\delta_{t+\Delta t}^{\max})$ is continuous with respect to d_0 . To accomplish this, we will use the *maximum theorem* [54]. This theorem states that if $\mathcal{Y}_0(d_0)$ is *continuous* with respect to

d_0 and *compact-valued*¹⁰, and $\delta_{t+\Delta t}^{\max}(y_0, t)$ is continuous in y_0 , then $\delta^{\max}(d_0, t)$ is continuous in d_0 .

$\mathcal{Y}_0(d_0)$ is continuous because the relationship between each y_0 and d_0 , i.e., the metric on \mathcal{L} , is continuous [52]. $\mathcal{Y}_0(d_0)$ is compact-valued if, for each d_0 , \mathcal{Y}_0 constitutes a compact set. Given that $\mathcal{Y}_0 \subset \mathbb{R}^n$, the *Heine-Borel theorem* [53] indicates that \mathcal{Y}_0 is compact if it is both closed and bounded. Every \mathcal{Y}_0 is closed as it fulfills an algebraic equation, and can be contained within any ball of radius larger than d_0 , making it bounded. Consequently, $\mathcal{Y}_0(d_0)$ is compact-valued.

Therefore, since $\delta_{t+\Delta t}^{\max}(y_0, t)$ is continuous with respect to y_0 , and $\mathcal{Y}_0(d_0)$ is both continuous and compact-valued, the maximum theorem states that $\delta^{\max}(d_0, t)$ is continuous with respect to d_0 . \square

Now, we can proceed to conclude about the continuity of β for both t and d_0 .

1. *Continuity in t* : For any given d_0 , since β evolves as a linear first-order system (as per (7)), its solution will exist provided that δ^{\max} is continuous with respect to t [55]. Then, under the assumptions of Prop. 1, Lemma 6 confirms that δ^{\max} is indeed continuous, provided that δ is continuous. From Lemma 5 we infer that δ is continuous with respect to t . Hence, β is well-defined for any given d_0 , indicating that it is differentiable with respect to t , and, therefore, continuous.
2. *Continuity in d_0* : For any given t , from (7), we know that β will be continuous with respect to d_0 as long as both of its terms, z_0 and the integral of \dot{z}_t , are continuous. The continuity of both terms depends on the continuity of δ^{\max} . Then, since Lemma 7 indicates that δ^{\max} is continuous with respect to d_0 provided that δ is continuous with respect to y_0 , and Lemma 5 confirms that this is indeed the case (given the assumptions of Prop. 1), we conclude that β is continuous with respect to d_0 .

d) $\beta \rightarrow 0$ as $t \rightarrow \infty$

To prove that this condition holds, we will utilize Lemma 8. The application of this lemma necessitates the use of Lemma 4 and Cor. 1, which are already introduced previously, and Lemma 9, which is introduced afterwards.

Lemma 8 (β converges to zero). $\beta \rightarrow 0$ as $t \rightarrow \infty$ if:

1. $\delta^{\max} \in [0, \max(\delta)]$,
2. δ^{\max} decreases with respect to t , $\forall d_0 \in \mathbb{R}_{\geq 0}$, $\forall t \in \mathbb{R}_{\geq 0}$,
3. $d_t < d_{t-\Delta t}$, $\forall y_0 \in \mathcal{L} \setminus \{y_g\}$, $\forall t \in \mathbb{R}_{\geq 0}$, (Theo. 4, 2).
4. δ^{\max} surjective in d_0 ,
5. $\delta^{\max}(0, t) = 0$, $\forall t \in \mathbb{R}_{\geq 0}$.

Proof. According to (8), β approaches δ^{\max} as $t \rightarrow \infty$. Thus, demonstrating that $\delta^{\max} \rightarrow 0$ as $t \rightarrow \infty$ would imply that $\beta \rightarrow 0$ as $t \rightarrow \infty$.

¹⁰The concepts of *compact-valued* and *continuous* refer to those employed in the literature of set-valued functions/correspondences. For further details, we refer the reader to [54].

Note that $\delta^{\max} \in [0, \max(\delta)]$ (condition 1) and δ^{\max} decreases for all t (condition 2). This indicates that as t goes to infinity, δ^{\max} must approach a limit $a \in [0, \max(\delta)]$. We will proceed to show that this limit can only be zero.

Let us define $y_0^* \in \mathcal{Y}_0$ and $t^* \in \mathbb{R}_{\geq 0}$ as the variables in (9) where the maxima are achieved for a given d_0 and t . Thus, $\delta^{\max} = \delta(y_0^*, t^*)$. From condition 3, we know that $\delta(y_0^*, t^* + \Delta t) < \delta(y_0^*, t^*)$, $\forall y_0^* \in \mathcal{L} \setminus \{y_g\}$, $\forall t^* \in \mathbb{R}_{\geq 0}$. This leads to two scenarios:

- i) y_0^* remains constant: If y_0^* does not change in the interval $[t, t^* + \Delta t]$, then $\delta(y_0^*, t^*)$, and therefore δ^{\max} , must strictly decrease at some point within this interval. Otherwise, $\delta(y_0^*, t^* + \Delta t) < \delta(y_0^*, t^*)$ would not hold true.
- ii) y_0^* changes: If y_0^* changes during the interval $[t, t^* + \Delta t]$, given that δ^{\max} decreases with t (condition 2), this change can only occur if $\delta(y_0^*, t^*)$, and hence δ^{\max} , strictly decreases at some point within the interval.

In either case, δ^{\max} strictly decreases at some point in the interval $[t, t^* + \Delta t]$, $\forall d_0 \in \mathbb{R}_{\geq 0} \setminus \{0\}$, $\forall t \in \mathbb{R}_{\geq 0}$.

Taking this into account, if the limit was some value $a \neq 0$, a contradiction would arise. If $a \neq 0$, we would always have a $d_0 \neq 0$ such that $\delta^{\max}(d_0, 0) = a$ (conditions 4 and 5). This implies that δ^{\max} must become lower than a before $t^* + \Delta t$, and, since it is decreasing (condition 2), it will remain lower as time progresses. Therefore, the only feasible value for the limit is $a = 0$, which confirms $\delta^{\max} \rightarrow 0$ as $t \rightarrow \infty$. Consequently, $\beta \rightarrow 0$ as $t \rightarrow \infty$. \square

Lemma 9 (δ^{\max} with d_0). $\delta^{\max} \in [0, \max(\delta)]$, and δ^{\max} surjective with respect to d_0 , if:

1. $\min(\delta^{\max}) = 0$,
2. δ^{\max} continuous with respect to d_0 .

Proof. Given that δ^{\max} computes a maximum over values of δ , we get $\max(\delta^{\max}) = \max(\delta)$. Then, we know that $\min(\delta^{\max}) = 0$ (condition 1), and that δ^{\max} is continuous with respect to d_0 (condition 2). Therefore, as a consequence of the *intermediate value theorem*, δ^{\max} can take any value between $\min(\delta^{\max})$ and $\max(\delta^{\max})$, i.e., $\delta^{\max} \in [0, \max(\delta)]$. Moreover, each value of $\delta^{\max} \in [0, \max(\delta)]$ must have at least one corresponding value of d_0 ; hence, in this interval, $\delta^{\max}(d_0, t)$ is surjective with respect to d_0 . \square

To summarize, given the conditions and assumptions of Prop. 1, Lemmas 4, 9 and Cor. 1, indicate that the conditions of Lemma 8 are fulfilled, implying that $\beta \rightarrow 0$ as $t \rightarrow \infty$.

e) β strictly increases with d_0

To prove this, we will introduce Lemma 10, which needs a condition supported by Lemma 11, introduced afterwards.

Lemma 10 (β strictly increases with d_0). β strictly increases with d_0 if:

1. z_0 strictly increases with d_0 ,
2. $\delta^{\max}(0, t) = 0$, $\forall t \in \mathbb{R}_{\geq 0}$,
3. β strictly decreases with t , $\forall d_0 \in \mathbb{R}_{\geq 0}$,

4. β continuous with t ,

5. $\beta \rightarrow 0$ as $t \rightarrow \infty$.

Proof. For a fixed t , the β strictly increases in d_0 if for any two numbers d_0^a and d_0^b (where $d_0^a < d_0^b$) within its domain, the condition $d_0^a < d_0^b$ implies $\beta^a(d_0^a, t) < \beta^b(d_0^b, t)$.

By condition 1, z_0 strictly increases with d_0 , so we have $z_0^a(d_0^a) < z_0^b(d_0^b)$. Moreover, since (any) z_0 is non-negative (see (10)), it follows that $z_0^b > z_0^a \geq 0$. Given condition 2, this indicates that $d_0^b > 0$.

Recalling (7), we have

$$\beta^b = z_0^b + \int_0^t \dot{z}_s ds.$$

Since $d_0^b > 0$, it follows from condition 3 that $\beta(d_0^b, t)$ strictly decreases with respect to t (i.e., $\dot{z}_t < 0$). Furthermore, β is continuous with t and approaches zero as time goes to infinity (conditions 4 and 5). This, combined with $z_0^b > z_0^a$, implies that there must exist a time $t^a > 0$ such that

$$\beta^b = z_0^b + \underbrace{\int_0^{t^a} \dot{z}_s ds}_{z_0^a} + \int_{t^a}^t \dot{z}_s ds. \quad (12)$$

Since $\dot{z}_t < 0$, starting from the same initial condition, a larger integration interval results in a smaller value of β . Therefore, we deduce that $\beta^b > \beta^a$, as β^a follows the same format as equation (12) (when replacing the terms equivalent to z_0^a , with z_0^b) but with an integral that starts at 0 instead of t^a , and $0 < t^a$. Thus, under the given conditions, β strictly increases with respect to d_0 . \square

Lemma 11 (z_0 strictly increases with d_0). z_0 strictly increases with d_0 if:

1. $\delta(y_0, t)$ continuous with respect to t .

Proof. For z_0 to strictly increase with d_0 , for any two numbers d_0^a and d_0^b within its domain, the inequality $d_0^a < d_0^b$ must imply $z_0^a(d_0^a) < z_0^b(d_0^b)$. From (10), we have $z_0 = \delta_0^{\max} + d_0$. Given that d_0 strictly increases with itself, it suffices to analyze the behavior of δ_0^{\max} .

Recall that $\delta_0^{\max} = \max_{y_0 \in \mathcal{Y}_0} (\delta_{t+\Delta t}^{\max}(y_0, 0))$ and that $\delta_{t+\Delta t}^{\max}(y_0, 0)$ computes the maximum over the set $\{\delta(y_0, s) : s \in [0, \Delta t]\}$. We will refer to this set as $\mathcal{W}(y_0)$. Importantly, $\mathcal{W}(y_0)$ contains $\delta(y_0, 0) = d_0$ for all y_0 . Then, for any d_0^a and d_0^b satisfying $d_0^a < d_0^b$, the behavior of δ_0^{\max} can be studied in three different scenarios. Let $y_0^a \in \mathcal{Y}_0(d_0^a)$ be the state that maximizes $\delta_{t+\Delta t}^{\max}$ for d_0^a , then:

i) $d_0^a = \delta_{t+\Delta t}^{\max}(y_0^a, 0)$: This scenario occurs when d_0^a is the maximum of $\mathcal{W}(y_0^a)$. Then, if $y_0^b \in \mathcal{Y}_0(d_0^b)$ is the state that maximizes $\delta_{t+\Delta t}^{\max}$ for d_0^b , and, hence, $d_0^b \in \mathcal{W}(y_0^b)$, the maximum of $\mathcal{W}(y_0^b)$ cannot be lower than d_0^b . Consequently, since $d_0^a < d_0^b$, we get $\delta_{t+\Delta t}^{\max}(y_0^a, 0) < \delta_{t+\Delta t}^{\max}(y_0^b, 0)$. As both y_0^a and y_0^b are those that maximize $\delta_{t+\Delta t}^{\max}$ over y_0 , for d_0^a and d_0^b , respectively, we conclude that $\delta_0^{\max}(d_0^a) < \delta_0^{\max}(d_0^b)$.

ii) $d_0^a < \delta_{t+\Delta t}^{\max}(y_0^a, 0) \leq d_0^b$: This scenario occurs when the maximum of $\mathcal{W}(y_0^a)$ is not d_0^a , and d_0^b is greater than or equal to this maximum. Following a similar reasoning to the above, we can conclude that $\delta_0^{\max}(d_0^a) \leq \delta_0^{\max}(d_0^b)$.

iii) $d_0^a < d_0^b < \delta_{t+\Delta t}^{\max}(y_0^a, 0)$: This scenario occurs when the maximum of $\mathcal{W}(y_0^a)$ is not d_0^a , and d_0^b is lower than this maximum. Provided that δ is continuous with t (condition 1), in the set $\mathcal{W}(y_0^a)$, since, for $t = 0$, $\delta = d_0^a$, and for some $t^* > 0$, $\delta = \delta_{t+\Delta t}^{\max}(y_0^a, 0)$, then we know there must exist a t^b , with $0 < t^b < t^* \leq \Delta t$, where $\delta = d_0^b$.

Now, observe that $t^* \in [t^b, t^b + \Delta t]$. Therefore, $\delta_{t+\Delta t}^{\max}(y_0^a, t^b)$, which computes the maximum over $\{\delta(y_0^a, s) : s \in [t^b, t^b + \Delta t]\}$, cannot be lower than $\delta_{t+\Delta t}^{\max}(y_0^a, 0)$. Moreover, we can select y_t^a at time t^b , i.e., $y_{t^b}^a$, as a new initial condition such that $\delta_{t+\Delta t}^{\max}(y_{t^b}^a, 0) = \delta_{t+\Delta t}^{\max}(y_0^a, t^b)$. Since $\delta(y_{t^b}^a, 0) = d_0^b$, we get that $y_{t^b}^a \in \mathcal{Y}_0(d_0^b)$. Hence, even though $y_{t^b}^a$ might not maximize $\delta_{t+\Delta t}^{\max}$ for $\mathcal{Y}_0(d_0^b)$, we know that the maximum, achieved at y_0^b , must be at least greater than or equal to $\delta_{t+\Delta t}^{\max}(y_{t^b}^a, 0)$.

Consequently, we have that $\delta_{t+\Delta t}^{\max}(y_0^b, 0) \geq \delta_{t+\Delta t}^{\max}(y_{t^b}^a, 0)$, and $\delta_{t+\Delta t}^{\max}(y_{t^b}^a, 0) = \delta_{t+\Delta t}^{\max}(y_0^a, t^b) \geq \delta_{t+\Delta t}^{\max}(y_0^a, 0)$. Hence, $\delta_{t+\Delta t}^{\max}(y_0^a, 0) \leq \delta_{t+\Delta t}^{\max}(y_0^b, 0)$, and, therefore, $\delta_0^{\max}(d_0^a) \leq \delta_0^{\max}(d_0^b)$.

In summary, for any d_0^a and d_0^b with $d_0^a < d_0^b$, it is always true that $\delta_0^{\max}(d_0^a) \leq \delta_0^{\max}(d_0^b)$, meaning δ_0^{\max} is non-decreasing with respect to d_0 . As the sum of a non-decreasing function (δ_0^{\max}) and a strictly increasing function (d_0) results in a strictly increasing function, we conclude that z_0 strictly increases with d_0 . \square

From Lemma 10, we can conclude that β strictly increases with respect to d_0 , since assuming the conditions of Prop. 1, and that we have proven that β is continuous in t , Lemmas 11, 3, and 8 indicate that the conditions of Lemma 10 are fulfilled.

To summarize, we have demonstrated that all the requirements for $\beta(d_0, t)$ to be a class- \mathcal{KL} function, and to serve as an upper bound for $\delta(y_0, t)$, are met for every $y_t \in \mathcal{L}$ and for all $t \in \mathbb{R}_{\geq 0}$. With this, our proof of Prop. 1 is complete. \square

B Learning on spherical manifolds

In this work, we employ unit quaternions to control orientation; therefore, we consider two distance functions that are relevant when learning spherical geometries: 1) great-circle distance, and 2) chordal distance.

- **Great-circle distance:** This is the distance along a *great circle*. A great circle is the largest circle that can be drawn on any given sphere, defining the shortest distance between two points. In the context of unit quaternions, which have a unitary norm, this distance is equivalent to the central angle α subtended by two points on the sphere. Hence, we can define it as

$$d_{\text{g.c.}} = \alpha.$$

- **Chordal distance:** This is a distance that can be computed when an n -sphere is embedded in a higher-dimensional Euclidean space, i.e., $\mathcal{S}^n \subset \mathbb{R}^{n+1}$. Then, by computing the Euclidean distance in \mathbb{R}^{n+1} between two points in \mathcal{S}^n , we *induce* a distance in \mathcal{S}^n , corresponding to the chordal distance [56, 57, 58]. As the name suggests, this distance is the length of the chord connecting two points in an n -sphere. Hence, it is defined as

$$d_{\text{chord}} = 2r \sin(\alpha/2),$$

where r is the radius of the n -sphere.

These distances are depicted in Fig. 15. Since both define the same topology \mathcal{S}^n they are considered to be equivalent, and can be utilized in PUMA to enforce stability when states are represented as unit quaternions. The great circle distance is especially suited to spherical spaces as it defines the *shortest path*, or the *geodesic*, between two points. Conversely, the chordal distance is straightforward to apply because it naturally arises when calculating the Euclidean distance at the output of ψ_θ . This is due to $\mathcal{L} \subset \mathbb{R}^m$, where $m > n$ represents the output size of ψ_θ .

B.1 Comments on local stability

Considering a one-dimensional sphere, it is notable that at $\alpha = \pi$ (with respect to the goal), both the great-circle distance and the chordal distance can decrease in two possible ways: by evolving either to the right or to the left (see Fig. 15). Consequently, to ensure these distances decrease in the region around $\alpha = \pi$, one of these options should be selected. However, this would require the dynamical system to instantly change its direction at this point, rendering f_θ^T discontinuous. Yet, in Theo. 4, we assume this function is continuous, as continuity is a prerequisite for the class- \mathcal{KL} upper bound β to also be continuous, which is necessary to prove stability.

Therefore, by extending this idea to higher-dimensional spheres, this implies that when employing these metrics, we can only enforce local asymptotic stability for $\mathcal{S}^n \setminus \{p\}$, where p is the point at $\alpha = \pi$. Moreover, due to the continuity of f_θ^T , this point must correspond to a zero, and, therefore, represents an unstable equilibrium. This property is not a flaw in the great-circle distance or the chordal distance. Rather, it is a result of the topology of \mathcal{S}^n , which does not allow for the existence of a single stable equilibrium. This is a consequence of the Poincaré-Hopf theorem [59].

B.2 Pose Control

Until now, our discussion has centered on the applicability of our method for unit quaternions. However, practical control of a robot's pose requires simultaneous control of both its position (Euclidean) and orientation (non-Euclidean). This can be achieved by using a *product metric*, i.e., a metric resulting from the Cartesian product of spaces. In this case, we are looking at the product $\mathbb{R}^3 \times \mathcal{S}^3$.

A simple product metric is the sum of the metrics from each space in the product [46], e.g., $d_{\mathbb{R}^n} + d_{\mathcal{S}^n}$ for $\mathbb{R}^n \times \mathcal{S}^n$, where $d_{\mathbb{R}^n}$ is a distance in \mathbb{R}^n and $d_{\mathcal{S}^n}$ is a distance in \mathcal{S}^n . However, it is not straightforward to do this in \mathcal{L} without

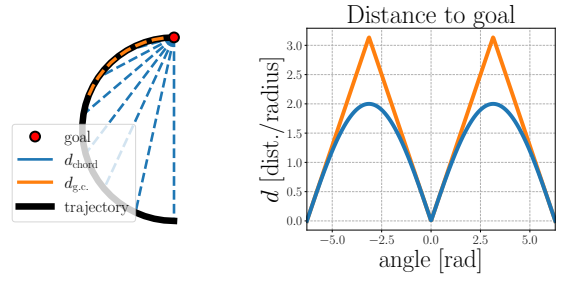


Figure 15: Left: A spherical trajectory towards a goal at the north pole. The chordal and great-circle distances at specific points are indicated as d_{chord} and $d_{\text{g.c.}}$, respectively. Right: Distances as a function of the central angle between points.

modifying the DNN structure. This is because the latent states y_t are an entangled representation of the robot states x_t , making it impossible to simply add together the distances of the Euclidean and non-Euclidean parts in the latent space.

Interestingly, when the product metric is computed using manifolds of identical topology, such as $\mathbb{R} \times \mathbb{R}$, the resulting metric is *equivalent* to the one obtained by directly computing the metric in the higher-dimensional space (\mathbb{R}^2 in this example) [46]. Hence, for such scenarios, there is no need to explicitly disentangle the states in \mathcal{L} ; instead, we can compute the metric directly in the complete latent space. Our case, nevertheless, is more complex since the topologies of \mathcal{S}^3 and \mathbb{R}^3 are different. Fortunately, we found two ways of easily overcoming this limitation.

B.2.1 Pose in Euclidean space

We have observed that an Euclidean metric, the chordal distance, can generate spherical metrics in lower-dimensional manifolds. This becomes particularly relevant when a Euclidean metric is employed in \mathbb{R}^m , where m exceeds the dimensionality of our state space (6 in our case). In this scenario, the metric is equivalent to $d_{\mathbb{R}^3} + d_{\mathbb{R}^{m'}}$ for $m' > 3$ and $3 + m' = m$. Given that \mathcal{S}^3 can be induced inside $\mathbb{R}^{m'}$, this suggests that $\mathbb{R}^3 \times \mathcal{S}^3$ can be induced in \mathbb{R}^m when using the Euclidean distance in this space.

B.2.2 Pose in spherical space

Finally, we also note that the great-circle distance can be employed to achieve the same objective. Suppose we compute this distance in \mathcal{S}^6 . Then, it would be equivalent to $d_{\mathcal{S}^3} + d_{\mathcal{S}^3}$. Interestingly, a diffeomorphism can be found between \mathbb{R}^n and a subset of \mathcal{S}^n , e.g., the *stereographic projection* [60]. This implies that it is feasible to use the metric $d_{\mathcal{S}^3}$ in \mathcal{L} , and find a valid representation for \mathbb{R}^3 within a subspace of \mathcal{S}^3 . Consequently, the product space $\mathbb{R}^3 \times \mathcal{S}^3$ can be represented within a subset of \mathcal{S}^6 .

C Hyperparameter Optimization

To optimize the hyperparameters of the different variations of PUMA employed in the LASA and LAIR datasets, we utilized

Table 4: Hyperparameter optimization results of the different variations of PUMA.

Hyperparameter	Opt.?	Hand-tuned value / initial opt. guess				Optimized value			
		Euc.	Sph.	Euc. (2nd order)	Sph. (2nd order)	Euc.	Sph.	Euc. (2nd order)	Sph. (2nd order)
CONDOR									
Stability loss margin (m)	✓	1.250e-8	1.250e-4	1.250e-4	1.250e-4	5.921e-3	3.012e-05	2.424e-08	2.919e-7
Triplet imitation loss weight (λ)	✓	1	1	1	1	1.315e-1	3.496	1.022e-1	4.473e-1
Window size imitation (\mathcal{H}^i)	✓	14	14	14	14	13	13	14	14
Window size stability (\mathcal{H}^s)	✓	4	1	1	1	11	13	11	11
Batch size imitation (\mathcal{B}^i)	✗	250	250	250	250	-	-	-	-
Batch size stability (\mathcal{B}^s)	✗	250	250	250	250	-	-	-	-
Neural Network									
Optimizer	✗	Adam	Adam	Adam	Adam	-	-	-	-
Number of iterations	✗	40000	40000	40000	40000	-	-	-	-
Learning rate	✓	1e-4	1e-4	1e-4	1e-4	9.784e-5	8.574e-4	1.670e-4	1.245e-4
Activation function	✗	GELU	GELU	GELU	GELU	-	-	-	-
Num. layers (ψ_θ, ϕ_θ)	✗	(3, 3)	(3, 3)	(3, 3)	(3, 3)	-	-	-	-
Neurons/hidden layer	✗	300	300	300	300	-	-	-	-
Layer normalization	✗	yes	yes	yes	yes	-	-	-	-

the Tree Parzen Estimator [61]. This optimization method builds a probability model that facilitates the selection of the most promising set of hyperparameters in each optimization round. For the implementation of the Tree Parzen Estimator, we used the Optuna API [62].

To evaluate the selected sets of hyperparameters, we employ a loss function $\mathcal{L}_{\text{hyper}}$ composed of two components. The first component, \mathcal{L}_{acc} , assesses the accuracy of the trained model. This is done by computing the RMSE between the demonstrations and the trajectories simulated by the learned model, in a manner similar to the approach used in the experiments section. The second component, $\mathcal{L}_{\text{goal}}$, quantifies the average distance between the final points of trajectories, simulated using the learned model, and the target goal. Thus, we have:

$$\mathcal{L}_{\text{hyper}} = \mathcal{L}_{\text{acc}} + \gamma \mathcal{L}_{\text{goal}}$$

where γ is a weighting factor. After initial tests, we settled on $\gamma = 3.5$.

To make the computationally intensive process of optimizing hyperparameters more feasible, we employed six strategies: 1) reducing the overhead of the objective function, 2) limiting the size of the evaluation set, 3) utilizing Bayesian optimization, 4) applying pruning techniques, 5) selecting a subset of hyperparameters for optimization, and 6) employing an optimization range. For details on the first five strategies, the reader is referred to [9]. The sixth strategy consists of restricting the hyperparameter search to a predefined range.

Table 4 presents the results of this optimization process. We can observe the hyperparameters that were optimized, their initial values (chosen based on preliminary tests), and their final optimized values. The ranges for hyperparameter optimization are as follows: 1) m : $[1e - 9, 1e - 1]$, 2) λ : $[1e - 1, 10]$, 3) \mathcal{H}^i : $[1, 14]$, 4) \mathcal{H}^s : $[1, 14]$, and 5) learning rate: $[1e - 5, 1e - 3]$. Note that the variations using the boundary loss are not included in the table, since in those cases the same hyperparameters were employed and the boundary loss was added with a weight of 0.001. The same holds for the behavioral cloning case. Lastly, regarding Sec. 4.4.2 it is important to note that in every experiment involving spherical state spaces, the dynamical system was kept within the manifold by normalizing the forward Euler integration output.

References

- [1] N. Perrin and P. Schlehuber-Caissier, “Fast diffeomorphic matching to learn globally asymptotically stable nonlinear dynamical systems,” *Systems & Control Letters*, vol. 96, pp. 51–59, 2016.
- [2] M. A. Rana, A. Li, D. Fox, B. Boots, F. Ramos, and N. Ratliff, “Euclideanizing flows: Diffeomorphic reduction for learning stable dynamical systems,” in *2nd Annual Conference on Learning for Dynamics and Control (L4DC)*, 2020.
- [3] J. Urain, M. Ginesi, D. Tateo, and J. Peters, “Imitation-Flow: Learning deep stable stochastic dynamic systems by normalizing flows,” in *2020 IEEE/RSJ International Conference on Intelligent Robots and Systems (IROS)*. IEEE, 2020, pp. 5231–5237.
- [4] S. M. Khansari-Zadeh and A. Billard, “Learning stable nonlinear dynamical systems with gaussian mixture models,” *IEEE Transactions on Robotics*, vol. 27, no. 5, pp. 943–957, 2011.
- [5] —, “Learning control Lyapunov function to ensure stability of dynamical system-based robot reaching motions,” *Robotics and Autonomous Systems*, vol. 62, no. 6, pp. 752–765, 2014.
- [6] A. Lemme, K. Neumann, R. F. Reinhart, and J. J. Steil, “Neural learning of vector fields for encoding stable dynamical systems,” *Neurocomputing*, vol. 141, pp. 3–14, 2014.
- [7] N. Figueroa and A. Billard, “Locally active globally stable dynamical systems: Theory, learning, and experiments,” *The International Journal of Robotics Research*, p. 02783649211030952, 2022.
- [8] A. Ude, B. Nemec, T. Petrić, and J. Morimoto, “Orientation in cartesian space dynamic movement primitives,” in *2014 IEEE International Conference on Robotics and Automation (ICRA)*. IEEE, 2014, pp. 2997–3004.
- [9] R. Pérez-Dattari and J. Kober, “Stable motion primitives via imitation and contrastive learning,” *IEEE Transactions on Robotics*, pp. 1–20, 2023.

- [10] J. Zhang, H. B. Mohammadi, and L. Rozo, “Learning riemannian stable dynamical systems via diffeomorphisms,” in *Conference on Robot Learning*, 2022.
- [11] J. Urain, D. Tateo, and J. Peters, “Learning stable vector fields on lie groups,” *IEEE Robotics and Automation Letters*, vol. 7, no. 4, pp. 12 569–12 576, 2022.
- [12] M. Saveriano, F. J. Abu-Dakka, and V. Kyrki, “Learning stable robotic skills on riemannian manifolds,” *Robotics and Autonomous Systems*, p. 104510, 2023.
- [13] F. Schroff, D. Kalenichenko, and J. Philbin, “Facenet: A unified embedding for face recognition and clustering,” in *Proceedings of the IEEE conference on computer vision and pattern recognition*, 2015, pp. 815–823.
- [14] M. Kaya and H. Ş. Bilge, “Deep metric learning: A survey,” *Symmetry*, vol. 11, no. 9, p. 1066, 2019.
- [15] S. Calinon, A. Pistillo, and D. G. Caldwell, “Encoding the time and space constraints of a task in explicit-duration hidden markov model,” in *2011 IEEE/RSJ International Conference on Intelligent Robots and Systems*. IEEE, 2011, pp. 3413–3418.
- [16] H. Ravichandar, A. S. Polydoros, S. Chernova, and A. Billard, “Recent advances in robot learning from demonstration,” *Annual review of control, robotics, and autonomous systems*, vol. 3, pp. 297–330, 2020.
- [17] A. J. Ijspeert, J. Nakanishi, H. Hoffmann, P. Pastor, and S. Schaal, “Dynamical movement primitives: learning attractor models for motor behaviors,” *Neural computation*, vol. 25, no. 2, pp. 328–373, 2013.
- [18] G. Li, Z. Jin, M. Volpp, F. Otto, R. Lioutikov, and G. Neumann, “Prodmp: A unified perspective on dynamic and probabilistic movement primitives,” *IEEE Robotics and Automation Letters*, vol. 8, no. 4, pp. 2325–2332, 2023.
- [19] H. B. Amor, G. Neumann, S. Kamthe, O. Kroemer, and J. Peters, “Interaction primitives for human-robot cooperation tasks,” in *2014 IEEE international conference on robotics and automation (ICRA)*. IEEE, 2014, pp. 2831–2837.
- [20] A. Pervez, Y. Mao, and D. Lee, “Learning deep movement primitives using convolutional neural networks,” in *2017 IEEE-RAS 17th international conference on humanoid robotics (Humanoids)*. IEEE, 2017, pp. 191–197.
- [21] R. Pahič, B. Ridge, A. Gams, J. Morimoto, and A. Ude, “Training of deep neural networks for the generation of dynamic movement primitives,” *Neural Networks*, vol. 127, pp. 121–131, 2020.
- [22] S. Bahl, M. Mukadam, A. Gupta, and D. Pathak, “Neural dynamic policies for end-to-end sensorimotor learning,” *Advances in Neural Information Processing Systems*, vol. 33, pp. 5058–5069, 2020.
- [23] N. Figueroa and A. Billard, “A physically-consistent Bayesian non-parametric mixture model for dynamical system learning,” in *Conference on Robot Learning*. PMLR, 2018, pp. 927–946.
- [24] H. Ravichandar, I. Salehi, and A. Dani, “Learning partially contracting dynamical systems from demonstrations,” in *Conference on Robot Learning*. PMLR, 2017, pp. 369–378.
- [25] K. Neumann and J. J. Steil, “Learning robot motions with stable dynamical systems under diffeomorphic transformations,” *Robotics and Autonomous Systems*, vol. 70, pp. 1–15, 2015.
- [26] J. Duan, Y. Ou, J. Hu, Z. Wang, S. Jin, and C. Xu, “Fast and stable learning of dynamical systems based on extreme learning machine,” *IEEE Transactions on Systems, Man, and Cybernetics: Systems*, vol. 49, no. 6, pp. 1175–1185, 2017.
- [27] H. Ravichandar and A. Dani, “Learning contracting nonlinear dynamics from human demonstration for robot motion planning,” in *Dynamic Systems and Control Conference*, vol. 57250. American Society of Mechanical Engineers, 2015, p. V002T27A008.
- [28] C. Blocher, M. Saveriano, and D. Lee, “Learning stable dynamical systems using contraction theory,” in *2017 14th International Conference on Ubiquitous Robots and Ambient Intelligence (URAI)*. IEEE, 2017, pp. 124–129.
- [29] W. Zhi, T. Lai, L. Ott, and F. Ramos, “Diffeomorphic transforms for generalised imitation learning,” in *L4DC*, 2022, pp. 508–519.
- [30] P. Pastor, L. Righetti, M. Kalakrishnan, and S. Schaal, “Online movement adaptation based on previous sensor experiences,” in *2011 IEEE/RSJ International Conference on Intelligent Robots and Systems*. IEEE, 2011, pp. 365–371.
- [31] L. Koutras and Z. Doulgeri, “A correct formulation for the orientation dynamic movement primitives for robot control in the cartesian space,” in *Conference on robot learning*. PMLR, 2020, pp. 293–302.
- [32] M. Lang and S. Hirche, “Computationally efficient rigid-body gaussian process for motion dynamics,” *IEEE Robotics and Automation Letters*, vol. 2, no. 3, pp. 1601–1608, 2017.
- [33] M. Arduengo, A. Colomé, J. Lobo-Prat, L. Sentis, and C. Torras, “Gaussian-process-based robot learning from demonstration,” *Journal of Ambient Intelligence and Humanized Computing*, pp. 1–14, 2023.
- [34] J. Silvério, L. Rozo, S. Calinon, and D. G. Caldwell, “Learning bimanual end-effector poses from demonstrations using task-parameterized dynamical systems,” in *2015 IEEE/RSJ international conference on intelligent robots and systems (IROS)*. IEEE, 2015, pp. 464–470.

- [35] I. Havoutis and S. Calinon, “Learning from demonstration for semi-autonomous teleoperation,” *Autonomous Robots*, vol. 43, pp. 713–726, 2019.
- [36] M. J. Zeestraten, I. Havoutis, J. Silvério, S. Calinon, and D. G. Caldwell, “An approach for imitation learning on riemannian manifolds,” *IEEE Robotics and Automation Letters*, vol. 2, no. 3, pp. 1240–1247, 2017.
- [37] S. Kim, R. Haschke, and H. Ritter, “Gaussian mixture model for 3-dof orientations,” *Robotics and Autonomous Systems*, vol. 87, pp. 28–37, 2017.
- [38] Y. Huang, F. J. Abu-Dakka, J. Silvério, and D. G. Caldwell, “Toward orientation learning and adaptation in cartesian space,” *IEEE Transactions on Robotics*, vol. 37, no. 1, pp. 82–98, 2020.
- [39] F. J. Abu-Dakka, Y. Huang, J. Silvério, and V. Kyrki, “A probabilistic framework for learning geometry-based robot manipulation skills,” *Robotics and Autonomous Systems*, vol. 141, p. 103761, 2021.
- [40] H. C. Ravichandar and A. Dani, “Learning position and orientation dynamics from demonstrations via contraction analysis,” *Autonomous Robots*, vol. 43, no. 4, pp. 897–912, 2019.
- [41] H. K. Khalil, *Nonlinear systems; 3rd ed.* Prentice Hall, 2002.
- [42] C. M. Kellett, “A compendium of comparison function results,” *Mathematics of Control, Signals, and Systems*, vol. 26, pp. 339–374, 2014.
- [43] T. Needham, *Visual Differential Geometry and Forms: A Mathematical Drama in Five Acts.* Princeton University Press, 2021.
- [44] I. Goodfellow, Y. Bengio, and A. Courville, *Deep learning.* MIT press, 2016.
- [45] A. Géron, *Hands-on machine learning with Scikit-Learn, Keras, and TensorFlow.* ” O’Reilly Media, Inc.”, 2022.
- [46] E. Deza, M. M. Deza, M. M. Deza, and E. Deza, *Encyclopedia of distances.* Springer, 2009.
- [47] S. Sommer, T. Fletcher, and X. Pennec, “Introduction to differential and riemannian geometry,” in *Riemannian Geometric Statistics in Medical Image Analysis.* Elsevier, 2020, pp. 3–37.
- [48] M. Müller, “Dynamic time warping,” *Information retrieval for music and motion*, pp. 69–84, 2007.
- [49] T. Eiter and H. Mannila, “Computing discrete Fréchet distance,” Technische Universitat Wien, Tech. Rep. CD-TR 94/64, 1994.
- [50] P. Corke and J. Haviland, “Not your grandmother’s toolbox—the robotics toolbox reinvented for python,” in *2021 IEEE International Conference on Robotics and Automation (ICRA).* IEEE, 2021, pp. 11 357–11 363.
- [51] V. I. Arnold, *Ordinary differential equations*, 3rd ed. Springer Science & Business Media, 1992, pp. 97–98.
- [52] J. R. Munkres, *Topology*, 2nd ed. Pearson Education, 2000, pp. 119–126.
- [53] C. C. Pugh, *Real mathematical analysis*, 2nd ed., ser. Undergraduate Texts in Mathematics. Springer, 2015, pp. 81, 97.
- [54] K. C. Border, *Fixed point theorems with applications to economics and game theory.* Cambridge university press, 1985, pp. 53–66.
- [55] R. K. Nagle, E. B. Saff, and A. D. Snider, *Fundamentals of differential equations*, 9th ed. Pearson, 2018, p. 53.
- [56] J. M. Lee, *Riemannian manifolds: an introduction to curvature.* Springer Science & Business Media, 2006, vol. 176.
- [57] C. Berg, *Complex Analysis.* Matematisk Afdeling, Københavns Universitet, 2008.
- [58] J. Jeong, M. Jun, and M. G. Genton, “Spherical process models for global spatial statistics,” *Statistical science: a review journal of the Institute of Mathematical Statistics*, vol. 32, no. 4, p. 501, 2017.
- [59] V. Guillemin and A. Pollack, *Differential topology.* American Mathematical Soc., 2010, vol. 370.
- [60] J. Oprea, *Differential geometry and its applications.* MAA, 2007.
- [61] J. Bergstra, R. Bardenet, Y. Bengio, and B. Kégl, “Algorithms for hyper-parameter optimization,” *Advances in neural information processing systems*, vol. 24, 2011.
- [62] T. Akiba, S. Sano, T. Yanase, T. Ohta, and M. Koyama, “Optuna: A next-generation hyperparameter optimization framework,” in *Proceedings of the 25th ACM SIGKDD international conference on knowledge discovery & data mining*, 2019, pp. 2623–2631.